FABRICATION AND CHARACTERIZATION OF TORSIONAL MICRO-HINGE STRUCTURES

A Thesis
presented to
the Faculty of California Polytechnic State University,
San Luis Obispo

In Partial Fulfillment
of the Requirements for the Degree

Master of Science in Engineering,
with Specialization in Materials Engineering

by
Mike Madrid Marrujo
June 2012

COMMITTEE MEMBERSHIP

TITLE: FABRICATION AND CHARACTERIZATION OF TORSIONAL MICRO-HINGE STRUCTURES

AUTHOR: Mike Madrid Marrujo

DATE SUBMITTED: June 6th 2012

Professor of Materials Engineering
Adviser and Committee Chair
Dr. Richard Savage

Professor of Electrical Engineering
Committee Member
Dr. Bill L. Ahlgren

Professor of Materials Engineering
Committee Member
Dr. Daniel W. Walsh

Fabrication and Characterization of Torsional Micro-Hinge Structures

Mike Marrujo

There are many electronic devices that operate on the micrometer-scale such as Digital Micro-Mirror Devices (DMD). Micro actuators are a common type of DMD that employ a diaphragm supported by torsional hinges, which deform during actuation and are critical for the devices to have high stability and reliability. The stress developed within the hinge during actuation controls how the actuator will respond to the actuating force. Electrostatically driven micro actuators observe to have a fully recoverable non-linear viscoelastic response. The device consists of a micro-hinge which is suspended by two hinges that sits inside a micro machined well. To achieve a specific angle of rotation when actuated, the mechanical forces need to be characterized with a range of different forces applied to the edge of the micro-hinge. This research investigates the mechanical properties and the amount of force needed to rotate to specific angles by comparing theoretical performance to experimentally measured values. Characterizing the mechanical forces on the micro-hinge will further the understanding of how the device operates under a specific applied force. The material response to the amount of stress within the hinges will control the amount of actuation that is achieved by that force. The test devices were fabricated using common semiconductor fabrication techniques. The micro-hinge device was created on a 500μm, double-sided polished, single crystal (100) silicon wafer. In order to create this device, both wet etching and dry etching techniques were employed to produce an 8μm thick plate structure. The bulk etching of 480μm was achieved by wet etching down into the silicon (Si) to create the wells. Dry etching was

used for its high precision to release the micro-hinge structure. Once fabricated, the micro-hinge actuators were tested using a Technics turntable arm with a built in micrometer that applied a constant force while measuring the displacement of the actuator. The rotation of the hinge was measured by reflecting a Helium-Neon (HeNe) laser beam off a mirror, which is attached to the pivot of the arm that's applying the force, and any type of displacement was recorded with a Photo Sensitive Device (PSD). The test stand applied a small force which replicated the amount of electrostatic forces needed to achieve a specific degree of rotation. Results indicate that the micro-hinge achieved a repeatable amount of rotation when forces were applied to it. The micro-hinge would endure deformation when too much force would be applied and yield a maximum amount of force allowed.

Keywords: MEMS, displacement, micro-hinge, repeatability, angle of rotation, torsional.

ACKNOWLEGEMENTS

I would first like to thank my supporting and loving family (Dan, Marion, and Daniel Marrujo), for giving me the love and support throughout my life and college years. Also I would like to thank God for the guidance and strength.

My advisor Dr. Savage, for his consistent support and advice in the development of this project and for always keeping the clean room stocked with the supplies needed.

Ladd Caine from the IME Department and John Sharpe from the Physics Department for helping me machine my test arm and helping with the optics for my test stand.

Nick Wiswell and Ross Gregoriev for their intellectual input and willingness to help.

Miranda Morgan for supporting me throughout the end of my master's program and willingness to proofread my final thesis paper.

Table of Contents

List of Figures

List of Tables

List of Equations

SECTION 1: INTRODUCTION

1.1 Background

MicroElectroMechanical Systems (MEMS) is a device combining electrical and mechanical components that are fabricated using integrated circuit (IC) batch processing techniques. MEMS are manufactured from a variety of materials and manufacturing methods. Materials used include semiconductors, plastics, ceramics, ferroelectric, magnetic, and biomaterials. In 1965, Gordon Moore made an observation: since the invention of the transistor in the late 1940s, the number of transistors per square inch on integrated circuits had doubled every 18 months after the creation of the IC. This observation captured the term "Moore's Law"[5]. Another notable scientist that predicted the emerging technology of smaller electromechanical systems was Richard Feynman. He was interested in exploring how to manipulate and control things on a small scale. Feynman was best known for his famous speech entitled: "There's Plenty of Room at the Bottom". Feynman said, "They tell me about electric motors that are the size of the nail on your small finger. It is a staggeringly small world that is below" [7]. These two men had the knowledge and foresight that the world was capable of having small scale devices and that society was inevitably headed in that direction. MEMS started to emerge in the semiconductor industry in the 1960's when sensors were integrated with circuits. Throughout the 1970's fabrication techniques used to create mechanical and electrical circuits on the micro scale were tested and perfected. It wasn't until the 1980's when MEMS started being mass produced to create sensors, actuators, accelerometers, switching, and light reflectors. MEMS devices range in size from a

millionth of a meter (micrometer) to a thousandth of a meter (millimeter). The core element in MEMS generally consists of two principal components, a sensing and/or an actuating element and a signal transduction unit [8]. There are two categories of inertial sensors, accelerometers and gyroscopes. The first measures variation of translational speed, while the other measures variation of rotational speed, respectively. The sensor is a device that converts one form of energy into another, and provides the user with a usable energy output in response to a specific measurable input. These sensors can be found in many places including biomedical practices for medical diagnosis purposes. An example would be a glucose sensor which is a MicroChemical sensor that consists of either an array of cantilevers or a single cantilever that detects and measures the amount of a specific substance like glucose in a sample. Each cantilever is coated with a chemically sensitive probe coating that attracts the glucose and allows for measuring the amount present. An actuator is another central type of MEMS which is designed to deliver a desired motion when driven by a power source [12]. The driving power for actuators varies depending on the specific applications. Actuation using electrostatic forces is essential when accurate and finite measurements are necessary. An electrostatic force can be defined as the electrical force of either repulsion or attraction induced by an electric field. One of the most commonly used optical MEMS devices is an electrostatically actuated micromechanical mirror. In such devices, voltages are applied to mirror electrodes to change the mirrors tilt angle. The mirror tilt angle is controlled by a balance between an electrostatic attractive torque and a mechanical restoring torque. As the voltage is increased, the electrostatic torque increases and eventually overcomes

the mechanical torque, causing the movable mirror to snap abruptly to the fixed electrode plane.

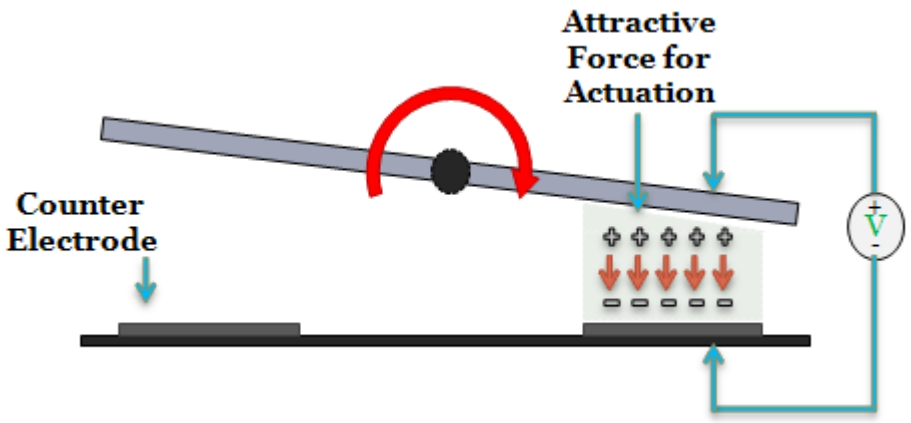

Figure 1 - Electrostatically actuated device

1.2 Motivation

Much of the motivation came from the past projects completed by Steven Meredith and Dylan Chesbro [22,23] that attempted to create a MEMS electro-static hinge structure that would rotate to a specific angle when a certain voltage load was applied to it. The hinge structure was able to rotate to a maximum angle of 0.019º and would drift closer over time to its starting angle of 0º. After researching the past projects that attempted this electro-static hinge, it was apparent that the force versus displacement was an important component, leaving the question as to why the hinge was unable to rotate to a more significant angle. In order to improve the performance of this electro-static hinge, the mechanical properties needed to be better understood and analyzed. Determining a force versus displacement will also help future students to understand the mechanics of these micro-hinges, and determine if the dimensions need to be changed for their application to become more successful. Micro-hinge structures are utilized within cell phones, tablets,

and medical applications. An example of this is the micro-hinge sensor that allows doctors to analyze certain elements within the human blood [20]. Based on the low manufacturing cost and ability to create repeatable measurements, micro-hinges have become one of the more popular MEMS devices currently in production.

SECTION 2: DESIGN AND OPERATION

2.1 Desired Analysis

It was vital to understand the mechanical property of a micro-hinge in order to understand the impact of electrostatics on a micro-hinge. The desired analysis was to test the micro-hinge with various forces, and determine the amount of rotation that corresponds with each force applied. The flexural strength or maximum strength of the micro-hinge needed to be determined, which corresponds to the amount of rotation the micro-hinge endures before failure. The micro-hinges must be able to rotate when the force is being applied and return to the exact position of 0° when the force is removed. The micro-hinge needed to rotate the same amount for a particular amount of force being applied in order to prove the repeatability of the micro-hinge. The dimensions for the micro-hinge were determined through Steven Meredith's thesis which proved to be successful [23]. It was also important to avoid deforming the micro-hinge while testing because this could result in inaccurate data. The micro-hinge endured multiple measurements with various amounts of force that were not to exceed the tensile strength of the silicon, avoiding permanent damage to the silicon. With a force applied the displacement was measured, ultimately providing the force versus displacement. In order to prevent damage to my devices, the test stand needed to be calibrated using a very sensitive scale designed to read small amounts of force on the order of thousandths of a gram. In order to measure

the mechanical properties of the micro-hinge a test stand needed to be developed that is capable of mounting each device accurately and test it repetitively. It was also necessary for the test stand to be in a fixed position and be capable of repeating the same amount of force during every test providing accurate data.

2.2 Actuation

The actuation of the micro-hinge needed to be forced to its maximum amount of rotation without causing the hinge to deform or snap. This was determined by analyzing the tensile strength of the silicon hinge. The tensile strength of a material is the maximum amount of tensile stress that it can be subjected to before failure. The failure will vary according to the type of material used and design methodology. Understanding the maximum amount of stress the hinge could endure helped to determine how much force needed to be applied to the hinge without damaging the micro-hinge during actuation. Using Equation 1 to determine the tensile strength would define how much force could be applied.

$$\sigma = \frac{F}{A_0} \tag{1}$$

The σ is the tensile strength, F is the amount of force being applied to the device in Newtons (N), and A_0 is the original cross-sectional area where the force is being applied in micrometers [14]. This was used to establish the sensitivity of the devices and determine the sensitivity of the test stand when applying a force.

2.2.1 Mechanical Forces

The mechanical portion of the device is the torsional hinge which is made of silicon. The hinge structure will feel resistance when a force is applied to the face of the plate. This can be accounted for by using Equation 2 Hooke's Law.

$$F_m = k\Delta d \tag{2}$$

Where F_m is the restoring force (N), k is the torsional spring constant of the hinge structure (N/m), and Δd is the change in distance (m) [14]. When a material is deformed beyond its elasticity limit, non-recoverable deformation will occur. The yield strength can be determined from the stress-strain curve also known as proportional limit. The stress-strain curve can be determined by measuring the load applied and by measuring the deformation of the sample. The slope of the stress-strain curve is called the tangent modulus, while the slope of the linear (elastic) portion is known as the Young's Modulus. The area under the curve will determine the materials modulus of resilience. The stress-strain curve was used to determine the amount of force that is tolerated and can be applied to the micro-hinge without fracturing the hinges. Silicon sensors are inherently very insensitive to fatigue failure when subjected to high cycle loads. The tensile strength is the stress at the maximum of the stress-strain curve. Both tensile strength and hardness are indicators of a metal's resistance to plastic deformation.

Plastic deformation in metals is based on the stress that is induced while a force is applied, which in turn create dislocations in the grain boundaries that migrate and form macroscopic deformation in the material.

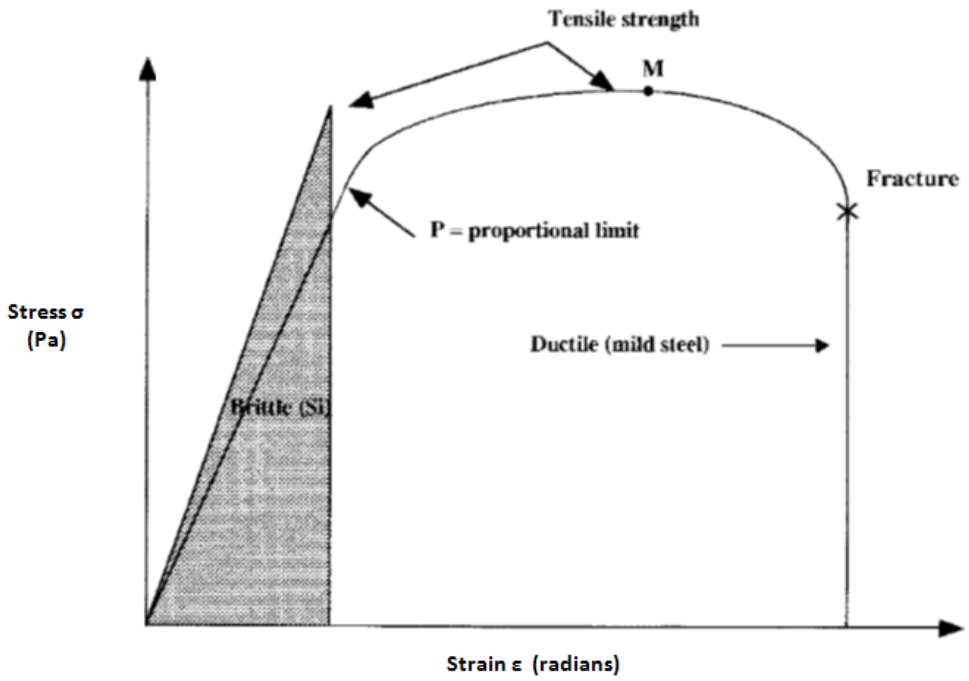

Figure 2 - Stress-strain curve for silicon (brittle) and mild steel (ductile)

Tensile strength and stress will vary between metals (observed in Figure 3). The amount of strain that Silicon can endure is much less than a more ductile material, causing it to fracture much sooner. Dislocations within the grain boundaries can cause permanent damage and non-repeatable results. Since these devices are required to perform multiple times, the repeatability to actuate the devices is crucial.

2.2.2 Mechanical Response

It was established that as the force is being applied, the stress of the micro-hinges will increase significantly at the hinges. Testing showed that the stress applied wasn't too significant to where the hinge structure was unable to return back to its original state. If the hinge structure is unable to return to its original state the micro-hinge would be considered flawed, rendering it incapable of being used in real life applications. In order

to avoid this type of deformation of the device, the total amount of force necessary had to be characterized using a highly sensitive milligram scale called the Mettler AE 160. Since the device is on the micron level, it would become very easy to damage the device with poor handling, or when applying a force to test and not damping the structure that's applying the force. Essentially, the test stand applying the force to the micro-hinge must slowly approach the device and apply the force with care. A damping mechanism would have to be determined before any testing could take place. The importance in having a damping mechanism is to avoid deformation on the micro-hinges while testing. The force applied needed to be controlled and stable at all times while testing the micro-hinge structures.

SECTION 3: FABRICATION

3.1 Overview

In order to create the actuators, a thermal oxide was grown on both sides of a double-sided polished wafer. Certain areas of this oxide were removed to expose the underlying silicon using the lithography process and etching techniques. The exposed areas were anisotropically etched at a rate of 24μm/hr which created wells approximately 490μm. Upon completing the etching into the silicon, a 9μm thick membrane was left. This process required delicate and sensitive handling while removing wafers from the wet silicon etchant, because repetitive testing showed that the water pressure can and will puncture through the membrane and destroy the device. The backside of the wafer had a grown oxide to pattern the actuator using lithography techniques. Reactive Ion Etching (RIE) was used to etch through the silicon membrane and to create the hinge structure in

the silicon. The research showed that RIE was preferred over wet etching because the gases didn't damage the hinge structure like wet chemicals did.

3.2 Thermal Oxidation

It was important to have a uniform oxide layer on each side of the wafer in order to create an etch mask. This etchant mask allows for certain areas to be exposed and others to be protected. Silicon dioxide was preferred over silicon because of its low etch rates. The low etch rate was important when etching through the entirety of the wafer.

The process began with soaking the wafer in piranha and Buffered Oxide Etch (BOE) to eradicate any surface contaminates and any oxide layer that may be present. Piranha is a 4:1 solution of sulfuric acid (H_2SO_4, 40%) and hydrogen peroxide (H_2O_2, 30%). When the solution is heated, it oxidizes organic matter and the silicon surface to leave an oxide layer. BOE, which contains sulfuric acid, is used to remove this layer of oxide to expose the bare silicon.

These wafers were placed in 70ºC piranha for ten minutes, rinsed with deionized (DI) water, and placed in BOE at room temperature for two minutes. The wafers were rinsed again with DI water and blown dry with low purity (LP) nitrogen. Next, the wafers were placed in a quartz boat with a dummy wafer at each end to ensure uniformity. The dummy wafers will help the uniform flow of gases and result in uniform oxide growth.

A thicker oxide layer was required to grow in order for the oxide to withstand a longer duration of wet etchant. Based on research, it has been proven that a 500nm thick oxide layer will suffice. The etch rate for silicon compared to silicon dioxide is referred to as

selectivity [21]. The silicon to oxide selectivity for 25wt% TMAH at 80ºC is more than 6000:1. The Deal-Grove Model in Equation 3 will determine the oxide growth that is required.

$$t + \tau = \left(\frac{X^2_o}{B} \right) + \left(\frac{X_o}{\left(\frac{B}{A} \right)} \right) \tag{3}$$

Where t is the oxidation time in hours, τ takes the initial oxide thickness into consideration, X_o is the oxide film thickness, B and B/A at 1050ºC are 0.35μm2/hr and 1.20μm, for (100) silicon and wet oxidation [22]. According to the Deal-Grove equation above, the time needed to grow a 500nm thick oxide would take 70 minutes at 1050ºC. Based on problems that were encountered with the furnace, the time to grow a 500nm thick oxide was actually 90 minutes at 1050 ºC using Mini Brute MB-81 furnace.

The process begins by preheating the furnace to 700ºC. Once the furnace reaches 700ºC, high purity nitrogen gas (99.999%) is pumped throughout the furnace tube. The wafers were then placed in the furnace tube and the temperature was raised to 1050ºC. When the temperature of the furnace reaches 1050ºC, high purity oxygen gas (99.999%) flows throughout the furnace tube to produce the desired oxide layer thickness. The high purity oxygen is pumped through deionized boiling water, which allows for water vapor to exist within the furnace tube. Once the oxidation process is completed, the furnace is shut off and the wafers are allowed to cool down to room temperature. Based on the evaluation the final oxide thickness range averaged from 480-500nm.

Table I - Wet sequence for thermal oxide growth in furnace

Process Steps	Temperatures	Gases
1. Preheat furnace	23ºc -700ºC	None
2. Insert wafer boat	700ºC	High purity N_2
3. Ramp up temperature	700ºc -1050ºC	High purity N_2
4. Expose for 130 minutes	1050ºC	High purity $O_2 + H_2O$
5. Cool down	1050ºC	High purity N_2
6. Cool down	700ºC	None

To determine the uniformity and thickness of the oxide that was grown, a film thickness measurement was taken using a Reflectometer called Filmetrics F20 tool.

Figure 3 - Measuring oxide growth thickness using filmetrics

An initial light is passed through the oxide thin film and the total thickness of the film is determined by the response of the reflected light, which is read using the Filmetrics software. The set up included first specifying what type of material is being used (Si)

and what kind of film is being analyzed (SiO_2). The light can be calibrated by shining the light directly off a pure silicon material, and also shining it off a known thickness that has the same oxide layer being used. The known oxide layer measured an 8142.7 Å thick oxide and when analyzing the sample it read an average of 8148 Å, which measures a difference of 3.5Å. This determined the oxide thickness of the wafer by shining and reflecting the light off its surface oxide layer. The difference of ±3.5Å should be considered as well when taking oxide measurements. To determine an average thickness, five different measurements were taken from the top, bottom, right, left, and center parts of the wafer with the primary flat facing down.

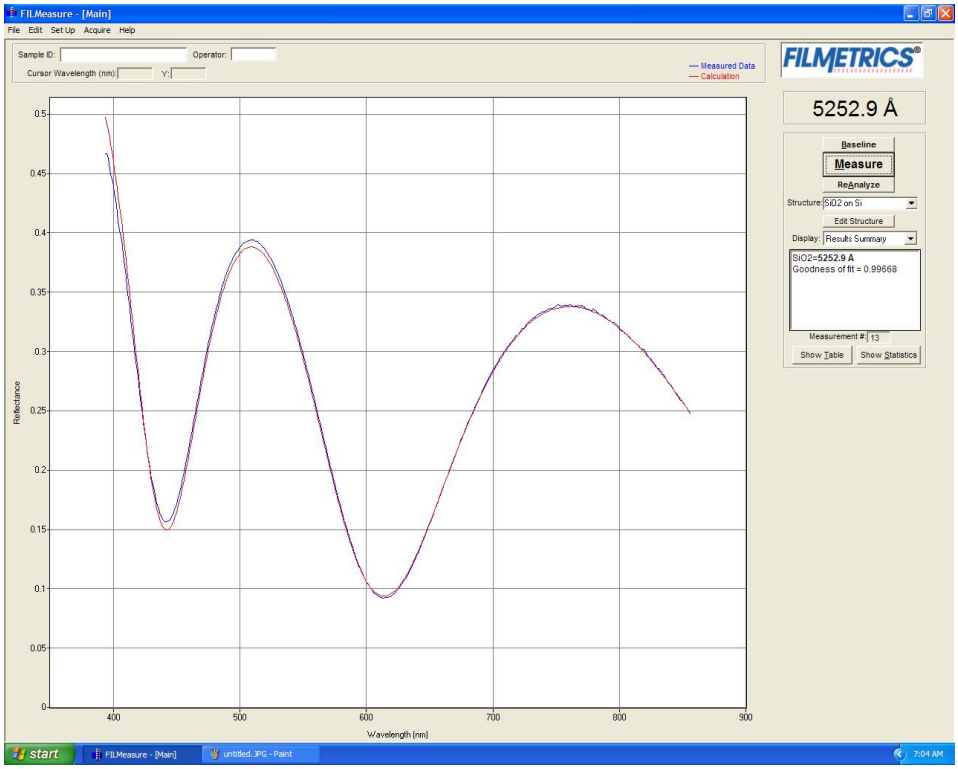

Figure 4 - Filmetrics SO_2 measurement (oxide thickness of 525.29nm)

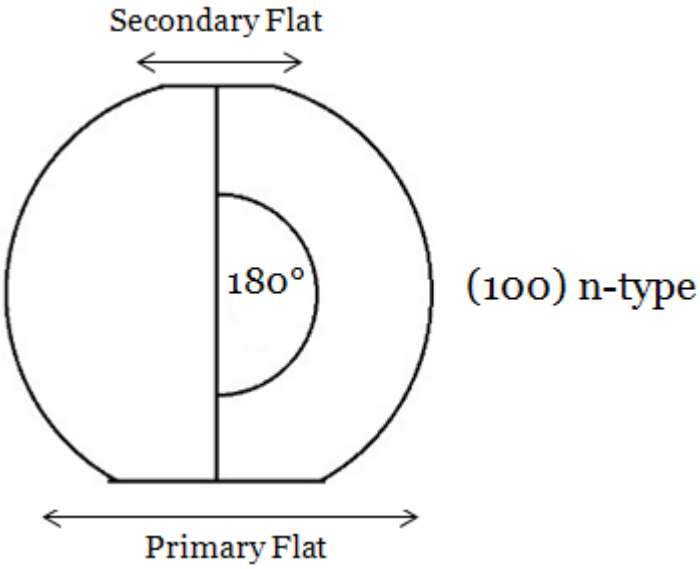

Figure 5 - Double sided (100) n-type wafer

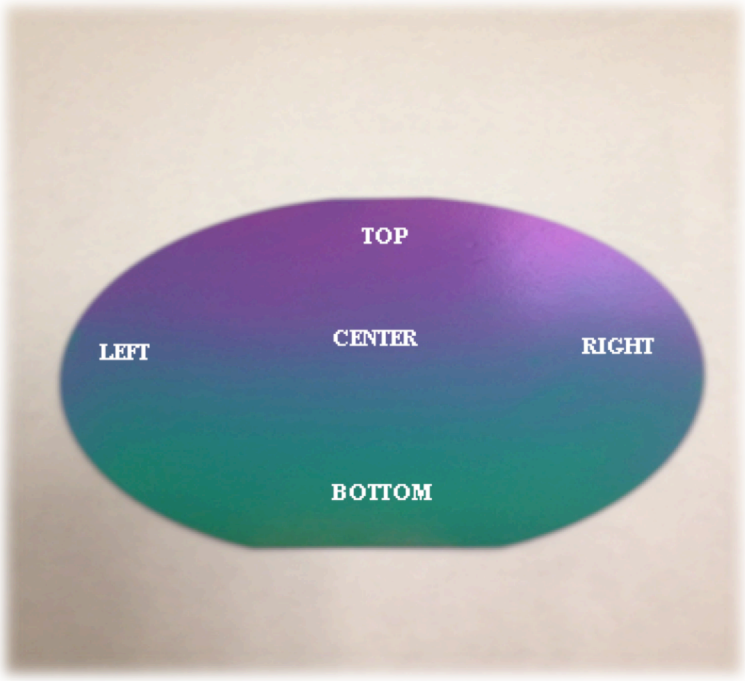

Figure 6 - Five quadrants of measurements using filmetrics

Table II - Filmetrics measurements for oxide growth

Measurement Position on Wafer	Oxide Thickness (nm)
1)Top	496.7
2)Bottom	497.2
3)Right	501.2
4)Left	496.2
5)Center	491
Average:	496.5

3.3 Positive Resist Photolithography and Bottom-Side Patterning

In order to expose silicon in specific areas, the oxide needed to be patterned. A photosensitive polymer was sputtered on the top surface of the oxide and patterned using standard lithography techniques.

Once the correct amount of oxide growth was achieved, the wafers were placed on a 150ºC hot plate to remove any residual moisture that could still be present. Once the wafers were cooled down and reached room temperature, they were placed in a Laurell Technologies WS-400B-6NPP spin-coater. First, a Micro Chemical (MCC) Primer 80/20 (4mL) was dispensed on the top surface of the wafer, which helped the adhesion between the positive resist and the substrate. It was necessary to use MCC primer and to remove any absorbed water. Subsequently, the Microposit S1813 positive photoresist was dispensed onto the wafer which ran through four different spin cycles (shown in Table III).

Table III - Positive photoresist spin-coating designed recipe

Process Steps	Spin Speed (RPM)	Time (Seconds)
1) MCC Primer Applied	250	25
2) MCC Primer	2000	20
3) Positive Photoresist Applied	200	20
4) Positive Photoresist	1000	5
5) Positive Photoresist	3000	15
6) Positive Photoresist	300	5

The first two process steps are to spread the MCC primer uniformly across the top surface of the wafer and to remove any moisture that may still be present. Process steps three, four, and five spread the positive resist, while step six creates a uniform layer of the positive resist. The final step slows down the chuck until it is brought to a complete stop.

Figure 7 - Positive photoresist chamber

The wafers were then soft baked on a 90ºC hot plate for 60 seconds to drive off any solvents and then cooled down for 30 seconds. The final thickness of positive resist was 2.8µm.

The wafers were then ready for lithography and were exposed to a Canon ultraviolet light.

Figure 8 - Photolithography aligner to expose UV light on substrate

The light integral was set at 4.5 which is16.7 seconds or 108mJ/cm^2. The first mask was used to expose the square membranes using the UV light. The wafers were then placed in 1165 Shipley developer for two minutes and soaked in DI water for one minute. The wafers were closely examined to ensure the correct pattern was achieved, and then hard baked at 150ºC on a hot plate for 60 seconds.

Figure 9 - Hot plates, soft baking (left) and hard baking (right)

Next, the wafers were placed back into the spin coater to cover the bottom side with positive photoresist using the same recipe as before, and once again hard baked on a 150ºC hot plate for one minute. It was important to coat the bottom side with photoresist to prevent any oxide from being removed when patterning the top side in BOE. Finally to complete the wafers process, they were submerged in BOE for 6.5 minutes to remove the exposed oxide and subsequently place in Shipley's photoresist stripper for two minutes to leave the square-patterned oxide film.

3.4 Wet Anisotropic Etching

To successfully create an 8µm hinge from a 500µm thick silicon wafer, the square membranes needed to be fabricated. The wafers were placed in a wet etchant, which etched anisotropically until only 8µm of silicon remained. The crystal planes in the monocrystalline silicon are what allow for the anisotropic etching to occur. Each crystal

plane has specific activation energies that can etch either faster or slower than others. The plane with the fastest etch rate or largest activation energy was (100) with the slowest being (111). The important etch plane is (111), which etches at a specific 54.74º angle and creates square wells.

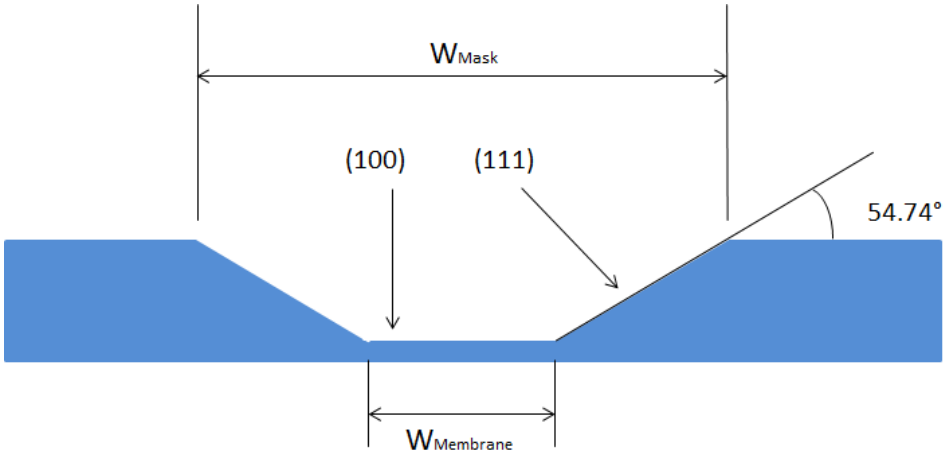

Figure 10 - Cross section of a (100) silicon wafer pit showing varying etch rates due to cryptographic planes

The wet etchant used was a 25wt% Tetra Methyl Ammonium Hydroxide (TMAH), and a water mixture of Isopropyl Alcohol (IPA) was added to the etchant at a 1:9 volume ratio. The reason for adding IPA was to create a more uniform etch rate over time. The solution was placed in a glass chamber and heated to 80ºC using an Omega heater that was equipped with a thermocouple, which maintained the temperature within the chamber. In order to assure the temperature within the chamber remained at 80ºC, the hot plate was set to 125ºC and the thermocouple was equipped with a feedback loop to keep track of the temperature during the process. The temperature within the chamber can be held at 80ºC ± 0.2ºC. The wafers were then placed in a Teflon cassette with the exposed silicon squares facing up. The stir bar was set at "1" which corresponds to 100RPM.

In order to determine an etch rate, the etched silicon wells were measured using Ambios XP-1 profilometer which can measure precisely down to 400µm. The stylus on the profilometer was dragged across the surface of the wafer, down into the silicon pit.

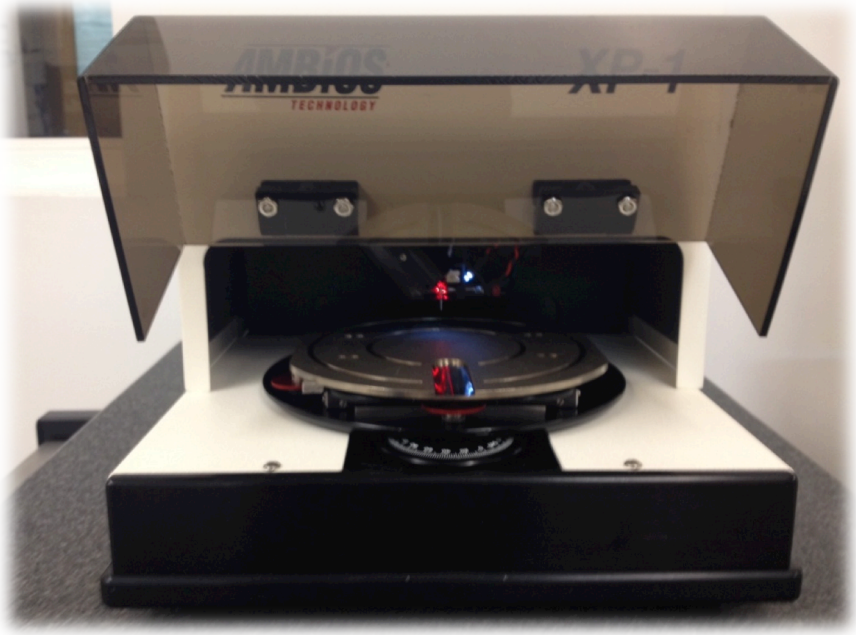

Figure 11 - Profilometer to measure Si etch depth

Numerous tests with multiple pits were measured and on average the etch rate of 24.5 ± 5.2µm/hr seemed to be the most repeatable etch rate, but it seemed to vary dramatically with each wafer being fabricated. The etch rate for each wafer also increased the further down the TMAH etched into the silicon wafer. The etch rate increased 9.464µm/hr and seemed to continue to increase, which made it difficult to know how far down it had etched over time.

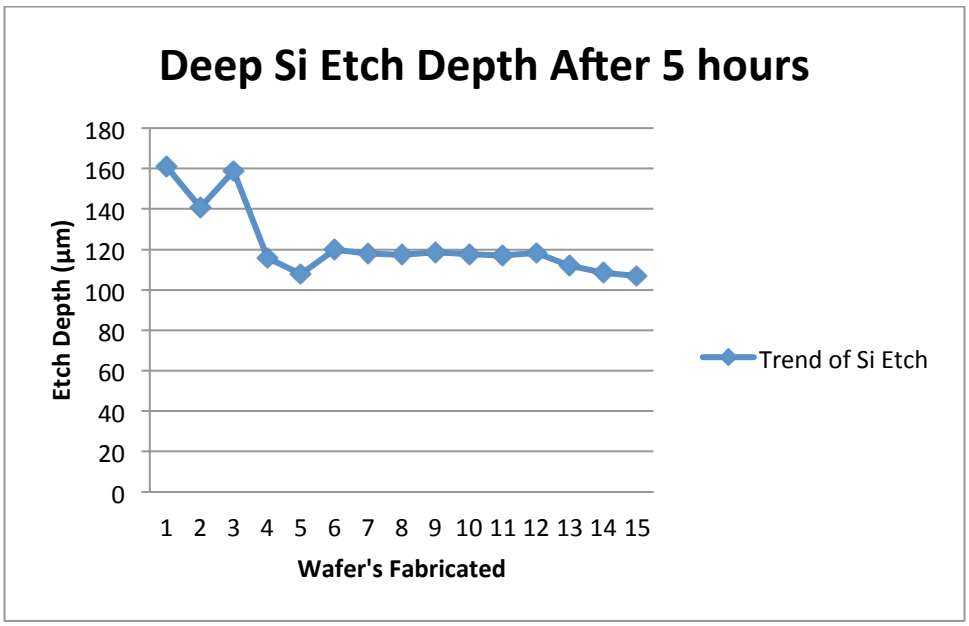

Figure 12 - Deep Si etch trend after 5 hours of exposure in TMAH measured with profilometer

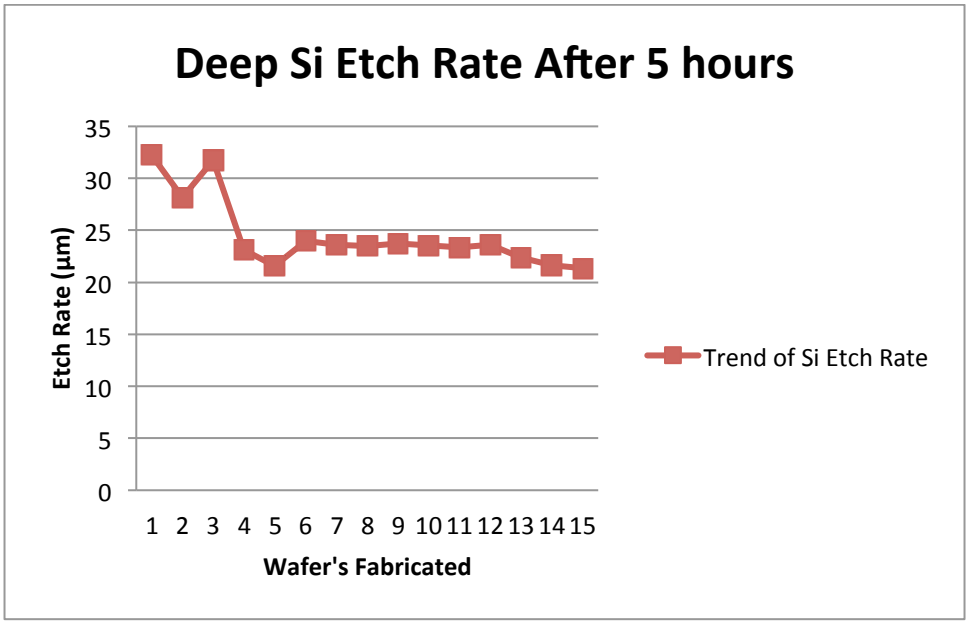

Figure 13 - Deep Si etch rate trend after 5 hours of exposure in TMAH measured with profilometer

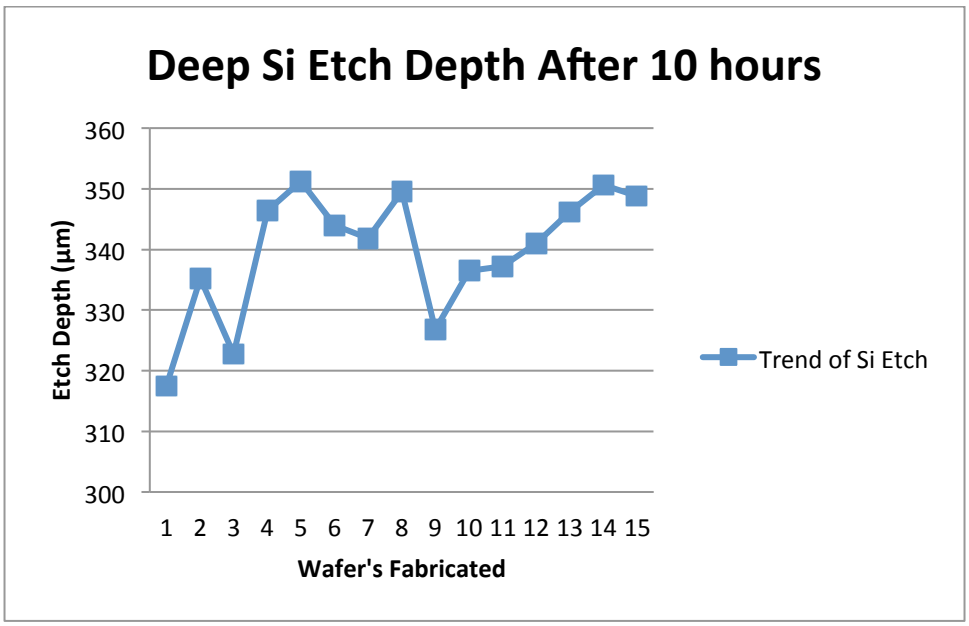

Figure 14 - Deep Si etch trend after 10 hours of exposure in TMAH measured with profilometer

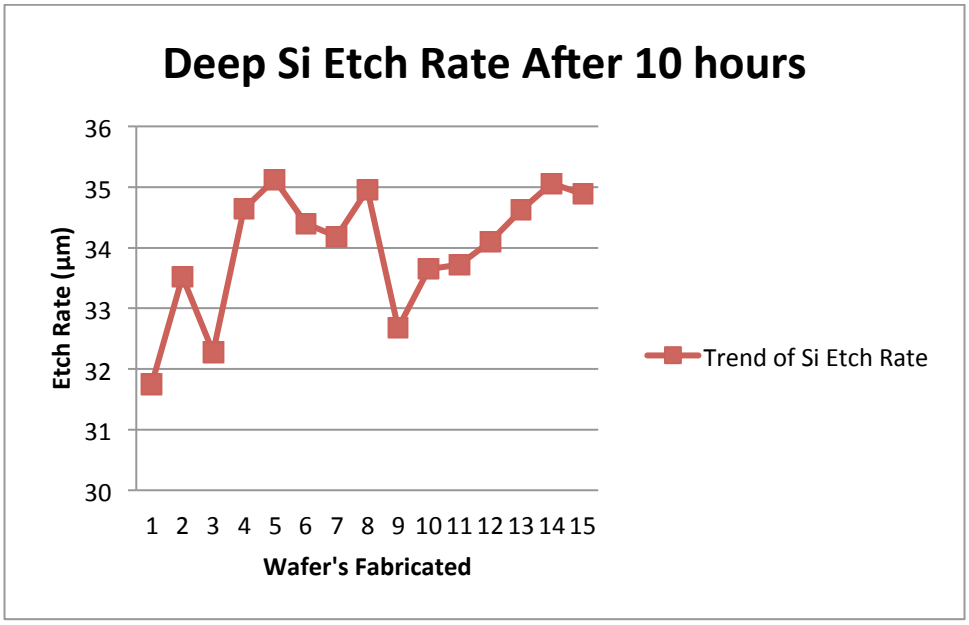

Figure 15 - Deep Si etch rate trend after 10 hours of exposure in TMAH measured with profilometer

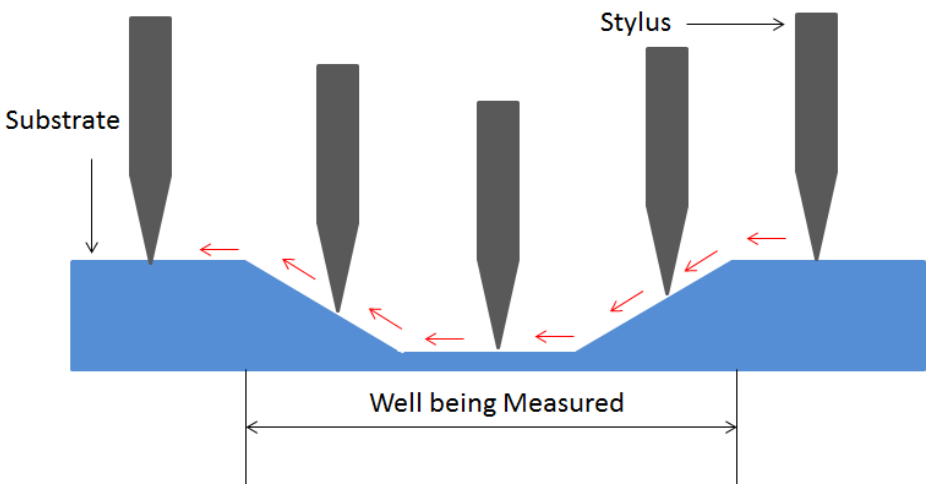

Figure 16 - Profilometer stylus measuring depth of well

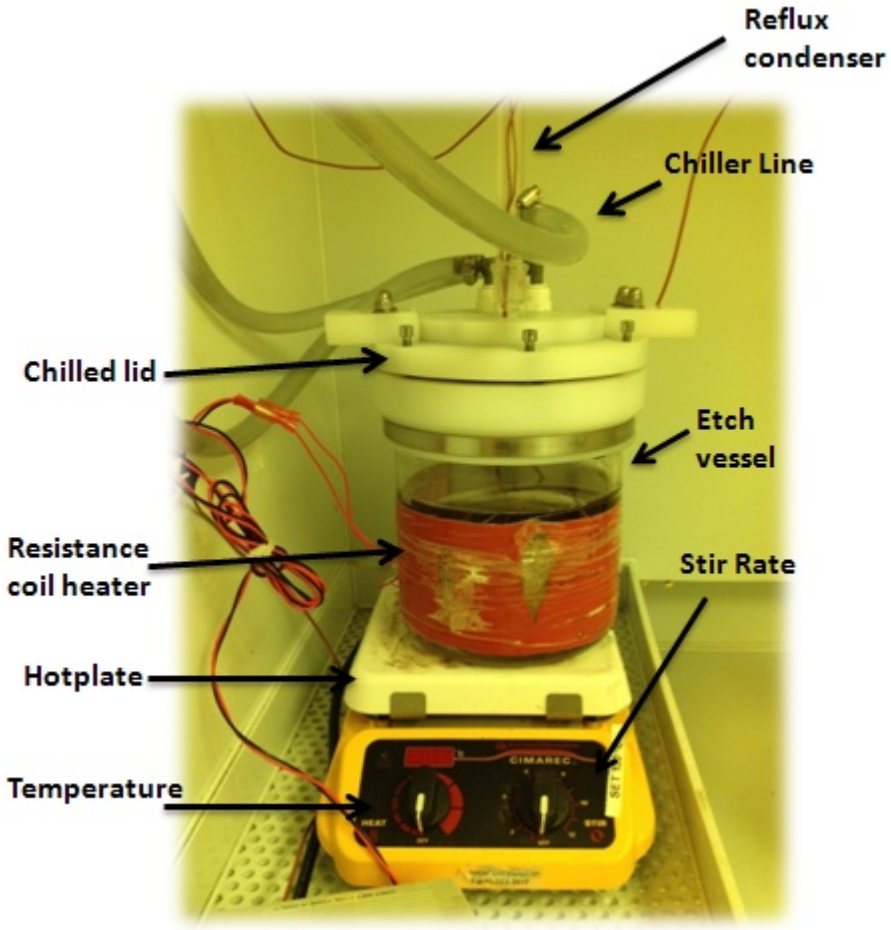

Figure 17 - Wet silicon etchant (TMAH) chamber to make silicon membranes

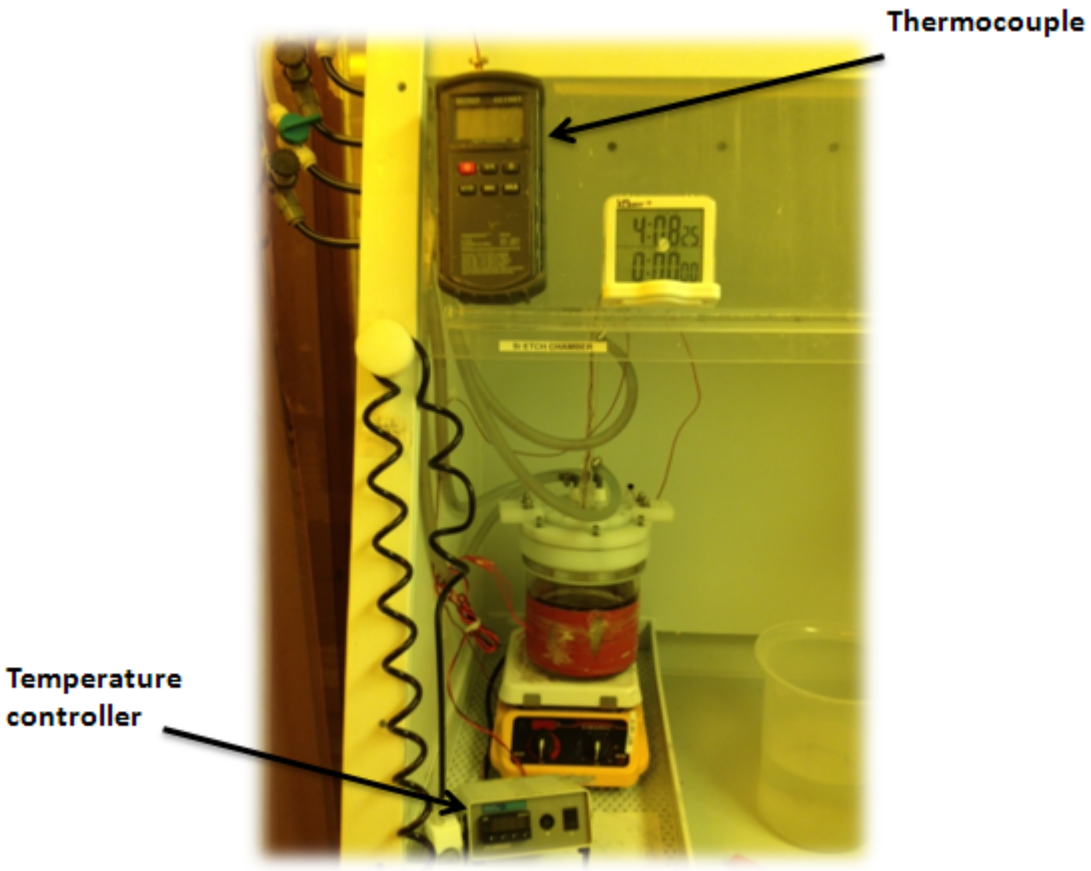

Figure 18 - Deep silicon etch temperature regulation

The profilometer was limited to measuring down to 400µm; therefore a new method for measuring membrane thickness had to be employed. This alternative method highlighted the anisotropic characteristics that silicon contains, producing different etch rates depending on the plane being etched. These membranes are etched at an angle, which allows for the use of geometry to determine the membrane thickness. An optical microscope and camera were used to focus on the top and bottom areas of the membrane to determine a working distance, which was used to calculate the depth of the membrane. The Olympus Optical Microscope was used to image the wells which allowed for geometry to determine the depths of the wells.

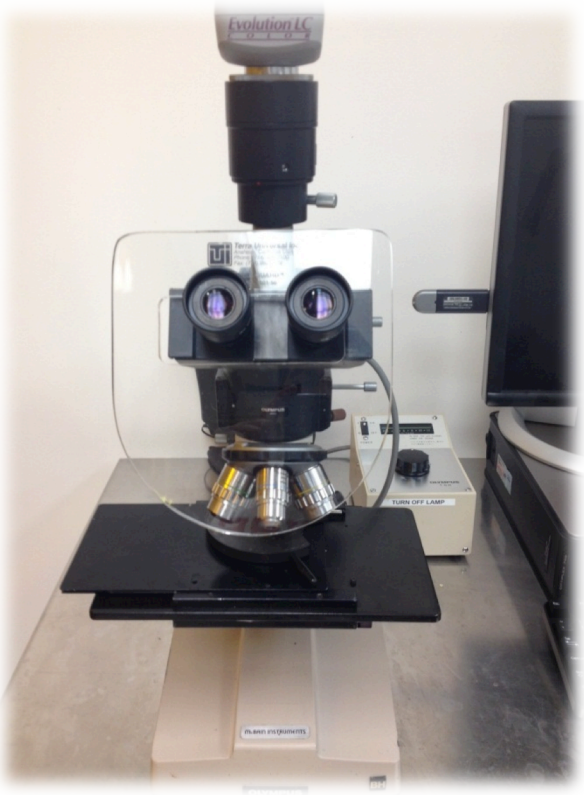

Figure 19 - The Olympus optical microscope used to measure depths of wells

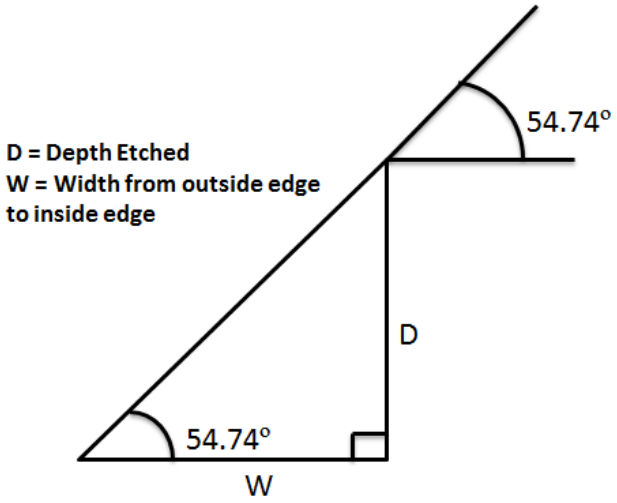

Figure 20 - Geometry ssed to determine Si etch depth

The depths from the optical microscope were compared to the profilometer measurement to insure accuracy and consistency. Using simple geometry, Equation 4 was used to determine the depth of the wells.

$$D = w * \tan(54.74°) \quad (4)$$

The D being the total depth that is etched down into the silicon thus far, while w is the width of the well from the outer edge to the inner edge. The equation uses the angle of 54.74°, which relates to the atomic organization of the crystallographic (111) plane.

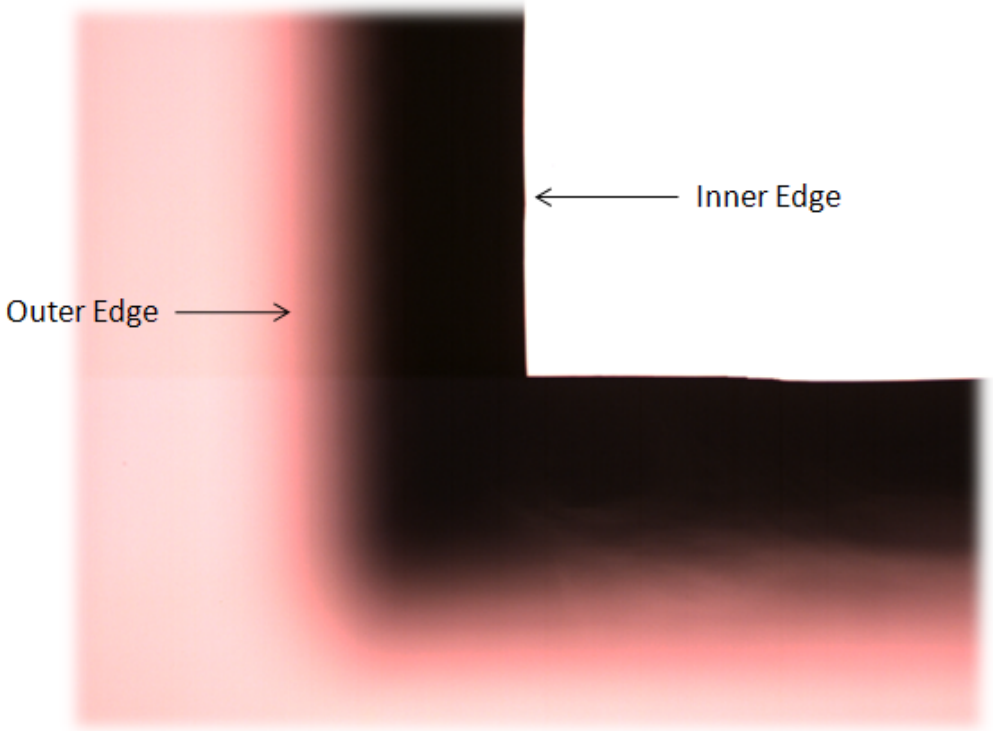

Figure 21 - Silicon inner edge focused from Olympus microscope

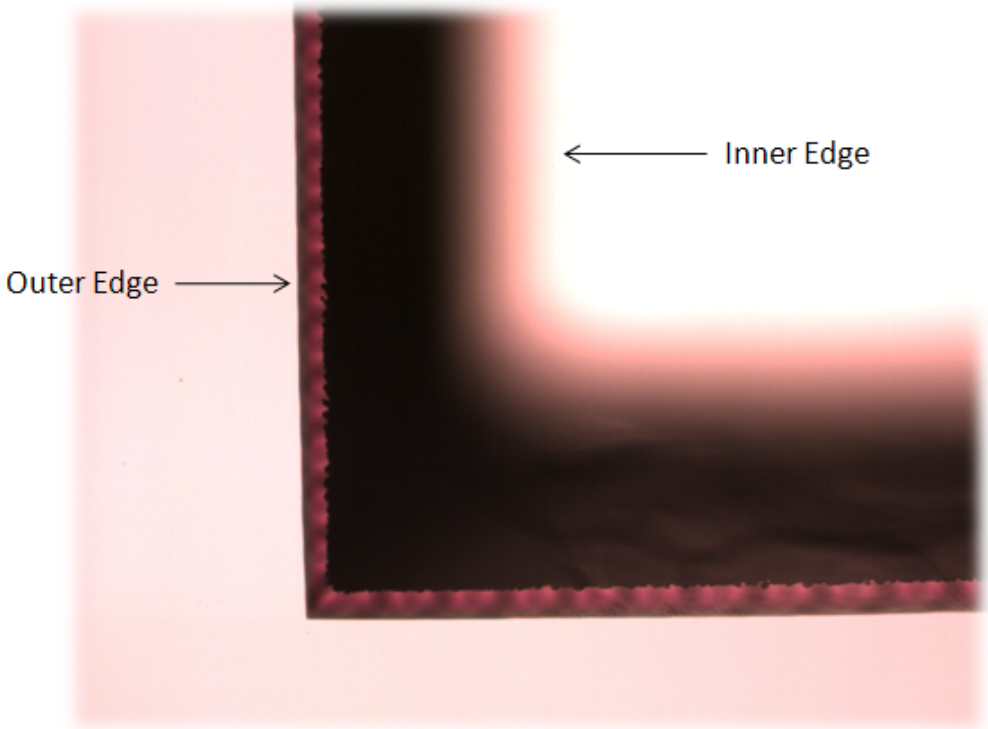

Figure 22 - Silicon outer edge focused from Olympus microscope

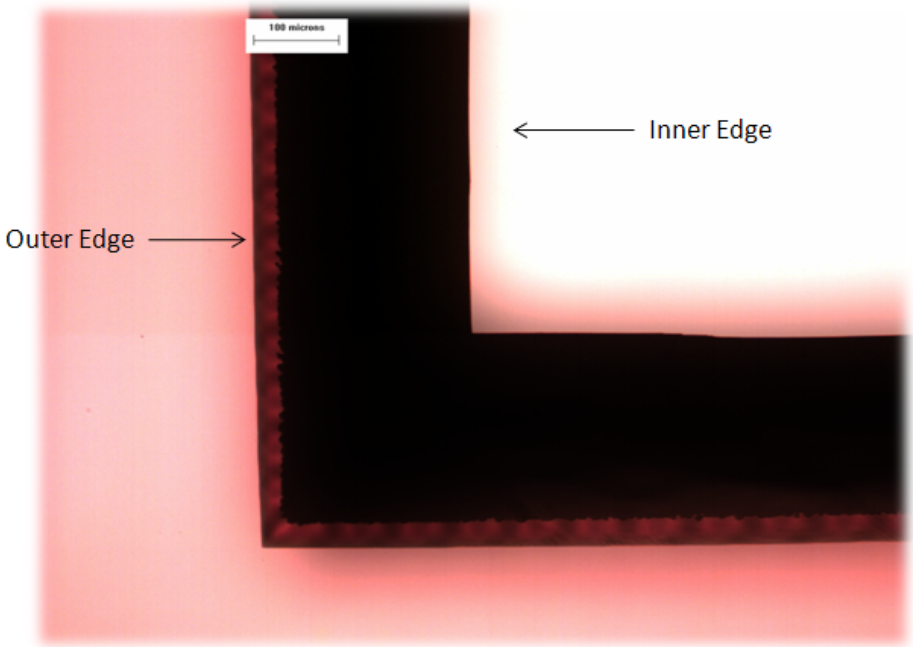

Figure 23 - Silicon overlay from Olympus microscope

One can see in Figure 24 that the TMAH etched a bit faster on the edges of the membrane, observed by the lighter color on the perimeter of the wells. This could have been due to either the temperature of the TMAH or the amount of voltage that rotates the spin bar within the chamber. To prevent this phenomenon, one can lower the temperature and the voltage that allows the stir bar to rotate.

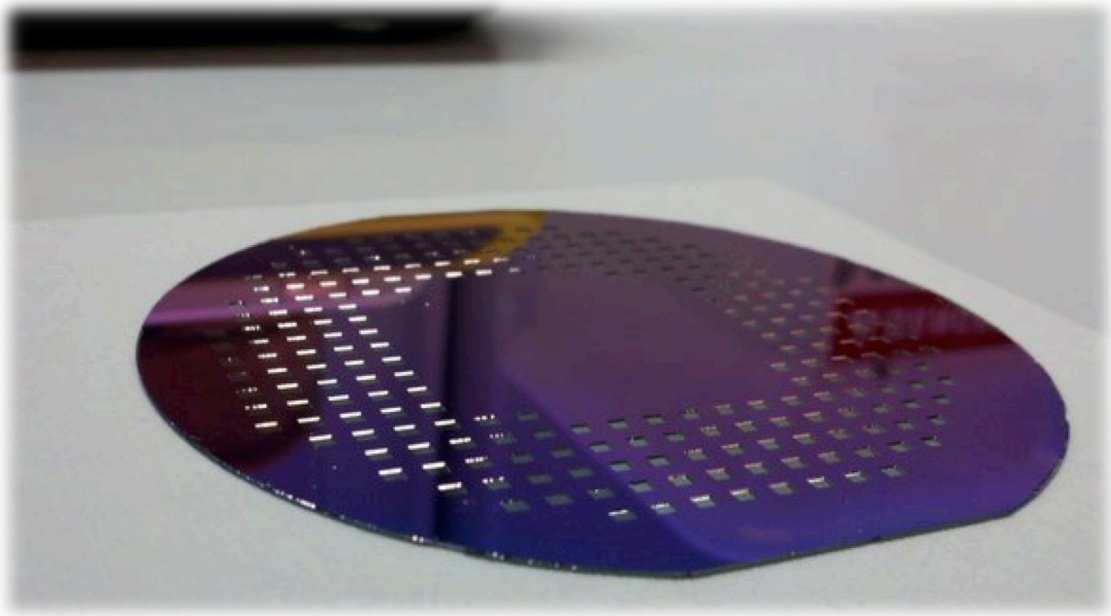

Figure 24 - Wells after deep silicon deep etch in TMAH

3.5 Top-Side Patterning And Dry Etching

In order to create the torsional hinge structure, the membranes needed to be patterned. This process was accomplished by patterning the top side oxide using similar lithography techniques described and employed in Section 3.3. The photoresist and oxide layer mask shown in Appendix A were used to transfer the pattern to the silicon membrane using RIE. This etched completely through the membrane, leaving just the hinge structure. With the membranes etched, the recipe described in Section 3.3 was altered to account for the pits that were created during the prior fabrication steps. The pits hampered the

flow of resist and prevented it from applying uniformly across the wafer during spin coating. While applying the photoresist it was important to change the acceleration speeds to not only create a uniform layer of photoresist but also to assure no damage to the wafer, as the wafers were very fragile due to the deep silicon etch. An issue identified during the lithography process, was the lack of alignment marks needed to align lithography mask II (seen in Appendix A) to the wafer. The membranes were not visible from the top side of the wafer, requiring repetitive attempts for successful alignment. Three membranes were purposely punched out to align the second mask and reveal the edges of the bulk silicon pits from the top side. The second mask was then meticulously aligned by hand using the punched out membranes as a reference.

The wet process required much more time and effort as the wafers became fragile due to the processing of multiple membranes in the silicon. The wafers were exposed, developed, and submerged in BOE to pattern the top oxide layer. Then the wafers were cleaned in DI water and dried on an 80ºC hot plate. In order to etch completely through the silicon to create the micro-hinge, the wafers were placed into the RIE chamber. The reason for using RIE etching opposed to wet etching was to avoid the undercutting caused by the isotropy of the etch.

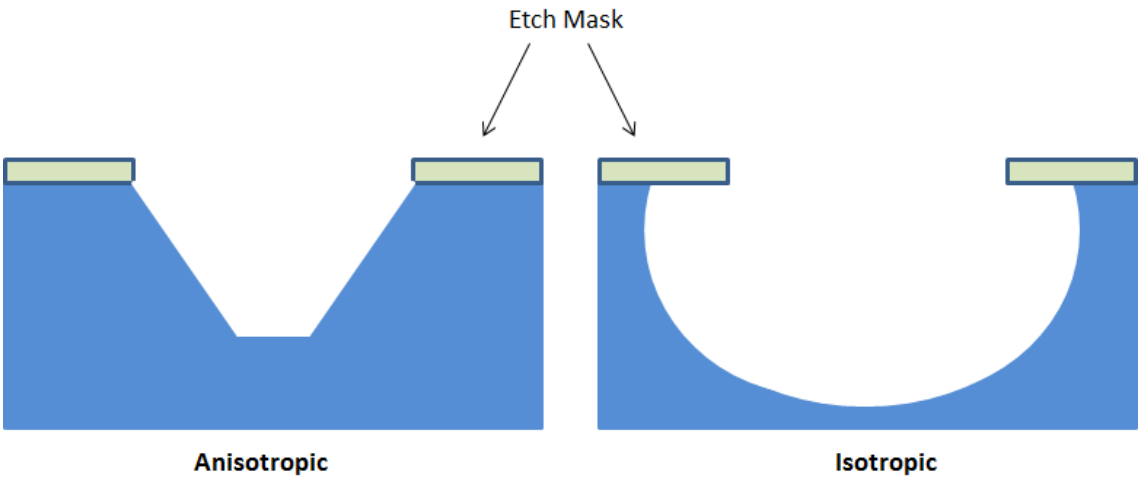

Figure 25 - Anisotropic (left) no undercutting and isotropic (right) undercutting

The purpose of dry etching is to create an anisotropic etch, which means that it will etch in a unidirectional manner.

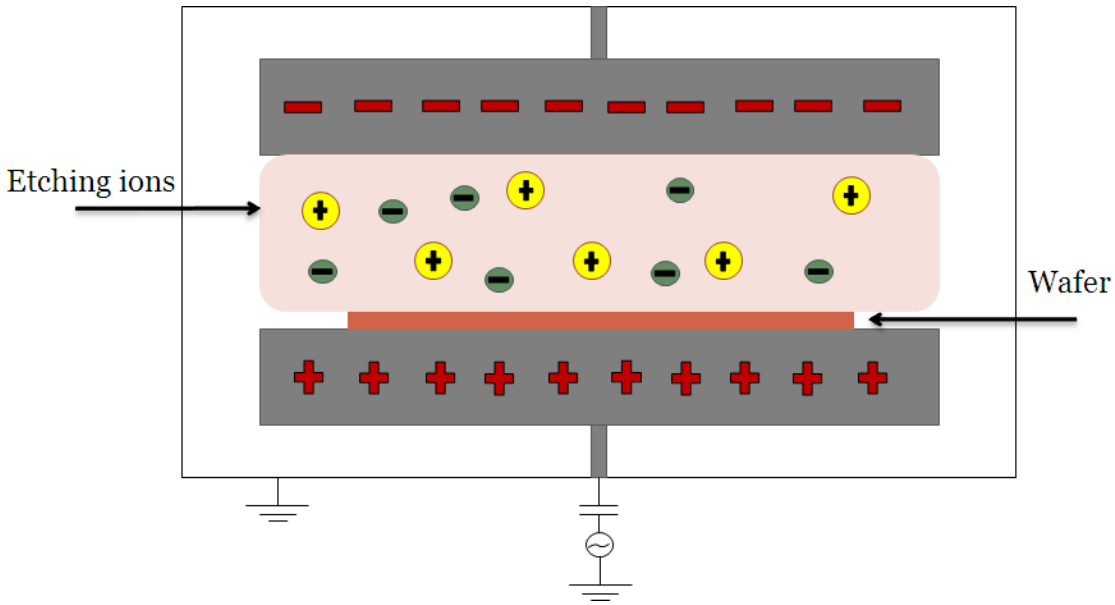

Figure 26 - RIE AG plasma system to release hinge structure

The RIE chamber was an important tool to use because of its high selectivity while etching anisotropically. The chamber consists of two electrodes that create an electric field designed to accelerate ions toward the surface of the sample. During this process the plasma is created by applying a Radio Frequency (RF) electromagnetic field to the

wafer. The oscillating electric field ionizes the gas molecules by stripping them of electrons, which creates the plasma.

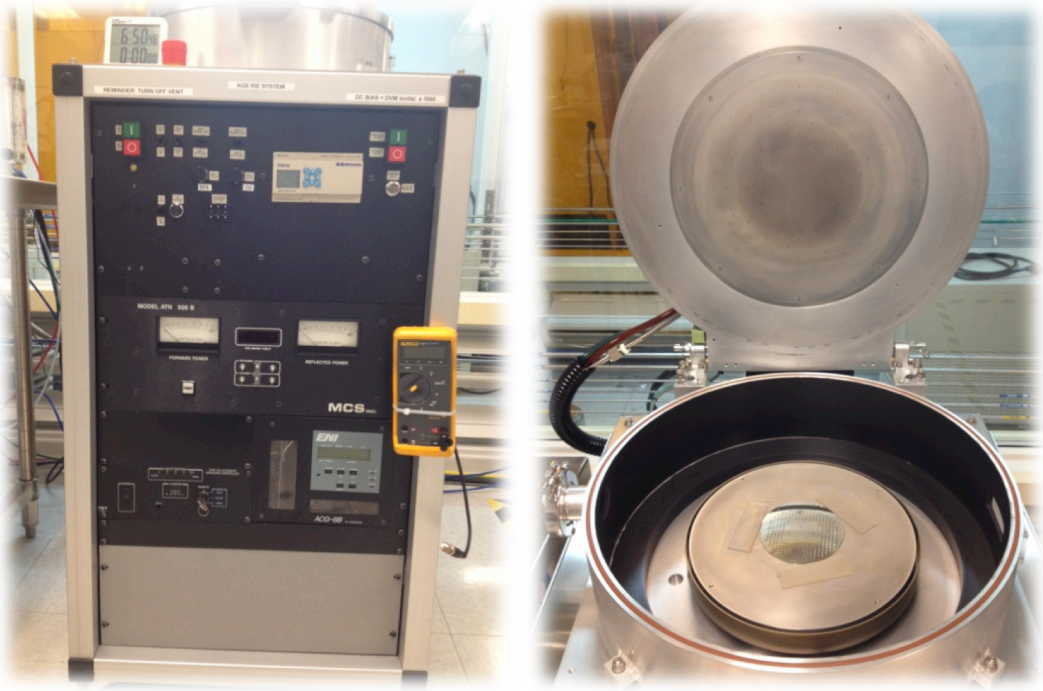

Figure 27 - RIE machine (left) and RIE chamber (right)

The gases used to create the plasma were Sulfur Hexafluoride (SF_6) and dioxide (O_2). Silicon begins to be removed when the SF_6 ions and radicals hit the silicon surface of the wafer. The final structure created is a torsional hinge.

Table IV - Specification for etching silicon with RIE

Gases	High Purity SF_6 and O_2
Mixtures	80:20
Pressure	300mTorr
Power	300W
Time	5 minutes

It became important to avoid overexposing the wafer which could cause charcoaling of the surface, or even worse etching the entire structure out of the membrane.

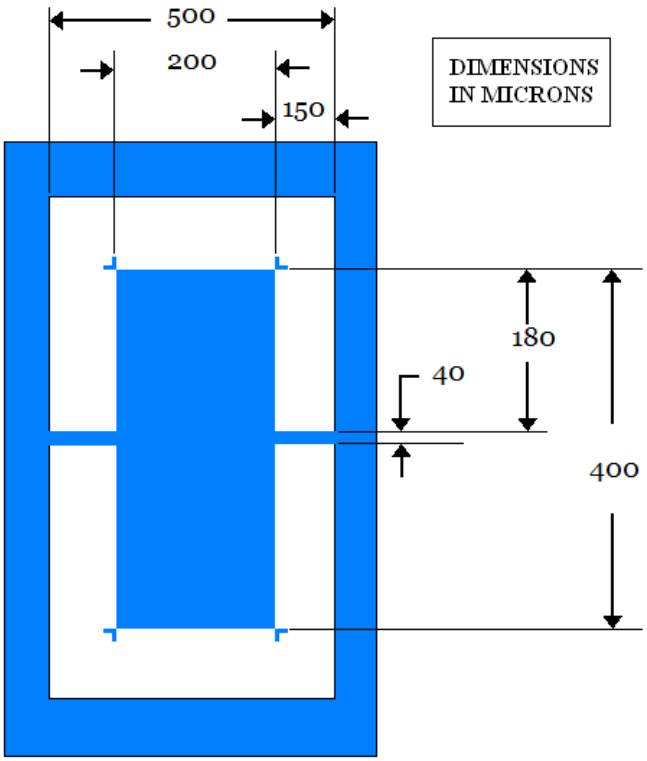

Figure 28 - Top view of the final silicon micro-hinge design with a thickness of 8µm

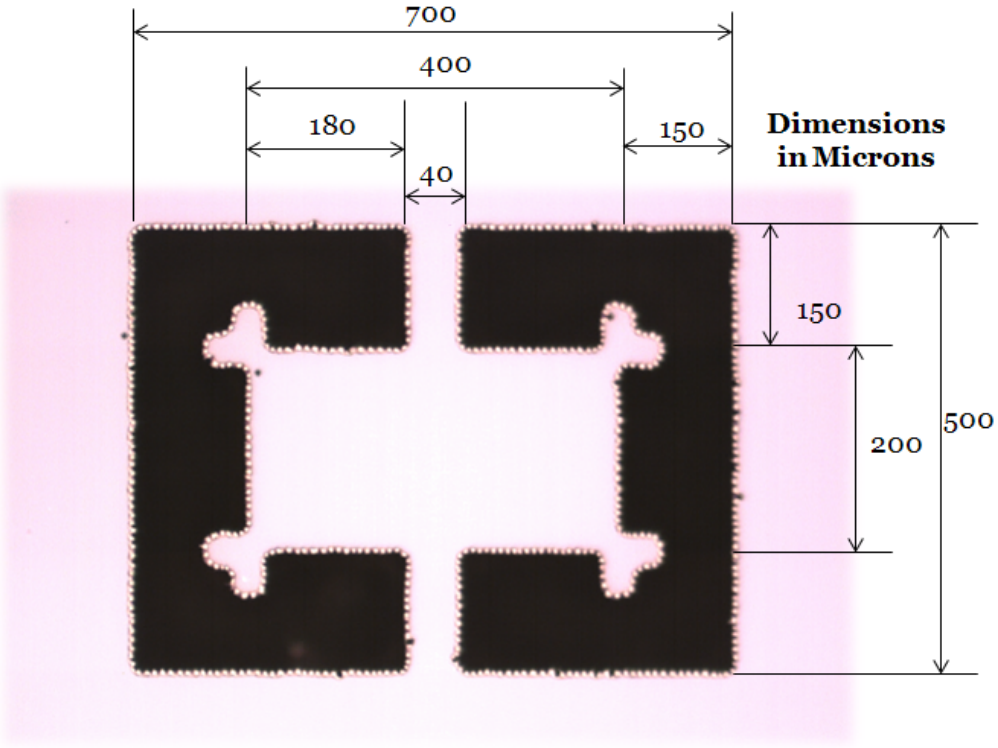

Figure 29 - Silicon micro-hinge structure from Olympus microscope with a thickness of 8µm

The final micro-hinge structure had 45° notches at each corner in order to help with aligning the array of micro-hinges to the wafer. However, the alignment could be done without the notches and seemed to have little significance.

3.6 Fabrication Issues

There were many obstacles encountered during the fabrication process that needed to be addressed and resolved. The largest concern was etching the silicon membranes to a specific depth without causing damage to the wafer, or etching too deep into the wafer. This issue was resolved by etching in smaller increments, rather than bulk etching for multiple hours at a time. Repetitive tests were conducted with varying time allowances to determine an etching rate that would sustain the calculated time tolerance, so that the wafers would not be damaged. Another issue arose during the lithography of my second mask on to the backside of the wafer. When masking the backside of the wafer with the hinge structure, the mask needed to be aligned with the previous membrane pattern. The issue was resolved by having three membranes effectively punched out around the wafer, resulting in alignment of the hinge structure within the membranes. There were also issues with the furnace not growing the calculated amount of oxide thickness, which was resolved with trial and error. The exposure time changed from two hours to two and a half hours to successfully grow a 500nm oxide thickness. Also while using the aligner, some adjustments needed to be made with inserting the wafer and recalculating the light integral. The aligner arm that picked up the wafer and inserted it into the machine for exposure stopped working and had to be resolved. In order to insert the wafer, an electrical component needed to be tripped to manipulate the aligner that a wafer was ready to be exposed. In addition, the UV light did not emit consistent light intensity

throughout my process which needed to be accounted for in my procedure. After calculating my original light integral of 4.5 which equals 16.7 seconds of exposure, an additional 3.71 seconds was added to account for the UV light intensity decreasing, which amounted to a total of 5.5 light integral, which is a total of 20.41 seconds of exposure.

SECTION 4: TESTING EQUIPMENT

4.1 Measurement Preparation

There were many methods used to test and observe the micro-hinges, tolerance, rotational characteristics, and deformation of the device. The main measurement taken was the force versus displacement. This was done to correctly characterize the micro-hinges response. The mechanical property of the micro-hinges was crucial to understand before performing any tests. These properties are more sensitive on the micron level the smaller the devices are. The properties of the materials change as their size approaches the micron or nano scale, and as the percentage of atoms at the surface of a material becomes significant. For bulk materials, the percentage of atoms at their surface is insignificant in relation to the number of atoms inside the bulk material. Once the material of the micro-hinge was defined, it was easier to determine the amount of force needed to rotate the hinge using a Finite Element Analysis (FEA) software. The tools used to determine this were Solid Works and Cosmos. I analyzed the model by first creating a virtual model in Solid Works, and then applying a pre-calculated load to this model to measure its stress and displacement using Cosmos. It was important to analyze the sample repetitiously, exactly the same way that was used to test; for example, applying the correct amount of force in the exact location of the device. If the force was not applied in the correct

location, it could have resulted in flawed data or unexpected stresses to occur during actual testing. To insure repeatable measurements, parts fabricated by Thorlabs were used to mount the test stand, while a Motion Controller/Driver Newport Universal was used to move the device directly in position for various tests for all of the devices. The direction of the force being applied was also important, as testing showed that I could not simulate applying a force at a slight angle. During the actual testing the applied force was placed directly perpendicular to the device. While performing this test the amount of ambient noise and outside interference played a factor in taking accurate measurements. To help eliminate some of the noise, the test stand was moved from the clean room into the Atomic Force Microscope (AFM) lab. Making sure that the device wafer and test stand were on a flat surface was equally very important, and the Thorlabs test bench proved to work well in creating this flat surface.

4.2 Measurement Methods

4.2.1 Atomic Force Microscopy Method

For the first method tested, I used a NanoSurf EasyScan 2 AFM to apply a force on the end of the micro-hinge using the stylus probe that is inserted into the AFM. An AFM is one kind of scanning probe microscopy that is designed to measure local properties using a probe. These local properties include, but are not limited to: height, friction, and magnetism. The AFM operates by measuring the force between the probe and the sample. Most AFM's use a laser beam deflection system, where a laser is reflected from the back of a cantilever head and onto a Position-Sensitive Detector (PSD). A cantilever

is a beam structure anchored at only one end and can be used for deflection when a load is applied at the end of the beam.

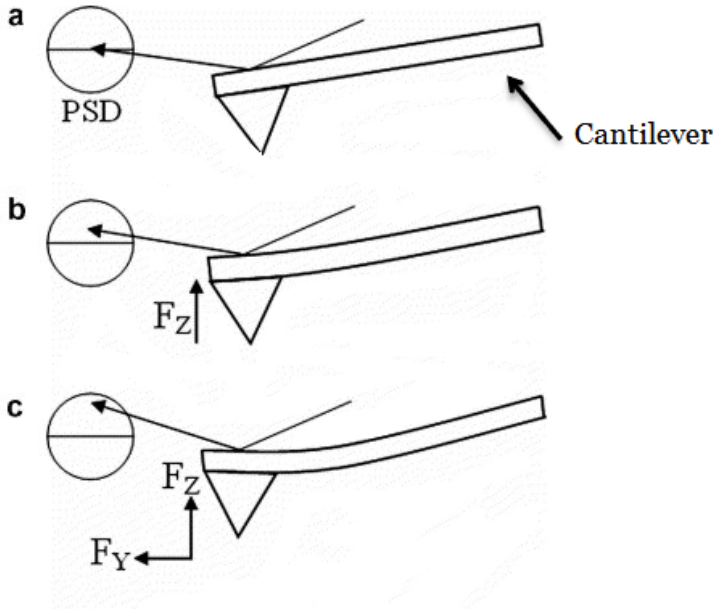

Figure 30 - Cantilever beam

Figure 31 - NanoSurf EasyScan 2 atomic force microscope

Since the AFM wasn't engineered to apply a force on something to measure its deflection, it was vital to know the amount of force that it could exert on something without damaging the stylus. The AFM was placed on micro controlled stages which could be programmed to move in the X or Y direction to position the AFM directly above the devices being measured. The two stages were mounted on a Thorlabs bench and stacked on top of each other to control the X and Y direction for positioning. The micro controlled stages could be calibrated to move one-hundred thousandth of a millimeter per increment. Being able to control how fast these micro controlled stages moved allowed the positioning to become rather simple. The complete wafer with all 153 devices was placed directly next to the micro controlled stages on top of two additional manually controlled stages, which would allow both the AFM and wafer to be at the same height.

The force can be calculated by measuring the deflection of the cantilever and knowing the stiffness of the cantilever.

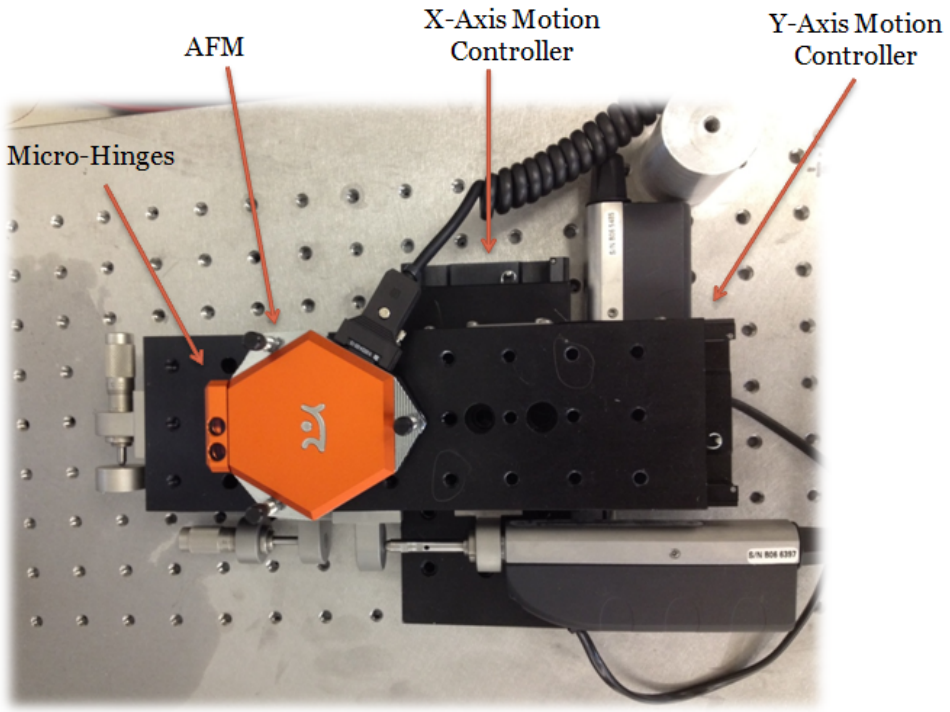

Figure 32 - AFM test stand

Since the AFM is primarily used to analyze the topography of a surface by scanning the surface with a very small amount of force, it was unable to apply enough force to the micro-hinge without snapping the stylus head in the AFM. The amount of force the AFM could apply to the devices ranged from 10^{-11} to 10^{-8} N/m. The tensile strength of the devices measured was much higher than the tensile strength of the stylus, leaving the stylus unable to rotate the devices at all. This method would have been very useful because lining up the stylus of the AFM over each device was straight-forward due to the two eye holes that allowed for both side and top views. These two eye holes assured that the force being applied was in the exact same location for all of the tests. Using the AFM to apply a force on smaller devices would have been more suitable due to the fact that the

stylus would have had a higher tensile strength. Thus another method was needed to apply a large enough force without damaging the test stand or the devices.

4.2.2 Micromanipulator And Micro Controlled Motors Method

This method involved using almost the same test stand as the AFM approach, but instead of using the AFM to apply the force, the micro controlled stages moved a small stylus directly into the edge of the micro-hinge. To determine the amount of force being applied, force was applied to a portable milligram scale before testing. The motion controller/driver was capable of converting the amount of movement in the X-axis to hundred thousandths of a millimeter, which proved to be a small enough movement in the X-direction to determine both the amount of rotation and the force being applied. Once the stylus applied a specific force on the bottom edge of the hinge, a HeNe laser was fixated through a focused lens, reflected off the top edge of the silicon micro-hinge, and read through a PSD. The HeNe cylindrical laser emits a beam at a wavelength of 632nm. The diameter of the HeNe laser beam was larger than the width of the micro-hinge and needed to be focused down using a focused lens, which allowed for better readings and less errors. A PSD is a diode that is sensitive to light in that when light increases, the diode resistance drops. The PSD was used to determine the change in resistance due to the amount of rotation the micro-hinge detects. It is able to measure the light intensity that is being reflected off the hinge. This method proved to work because the amount of force being applied was constant and repeatable for each test.

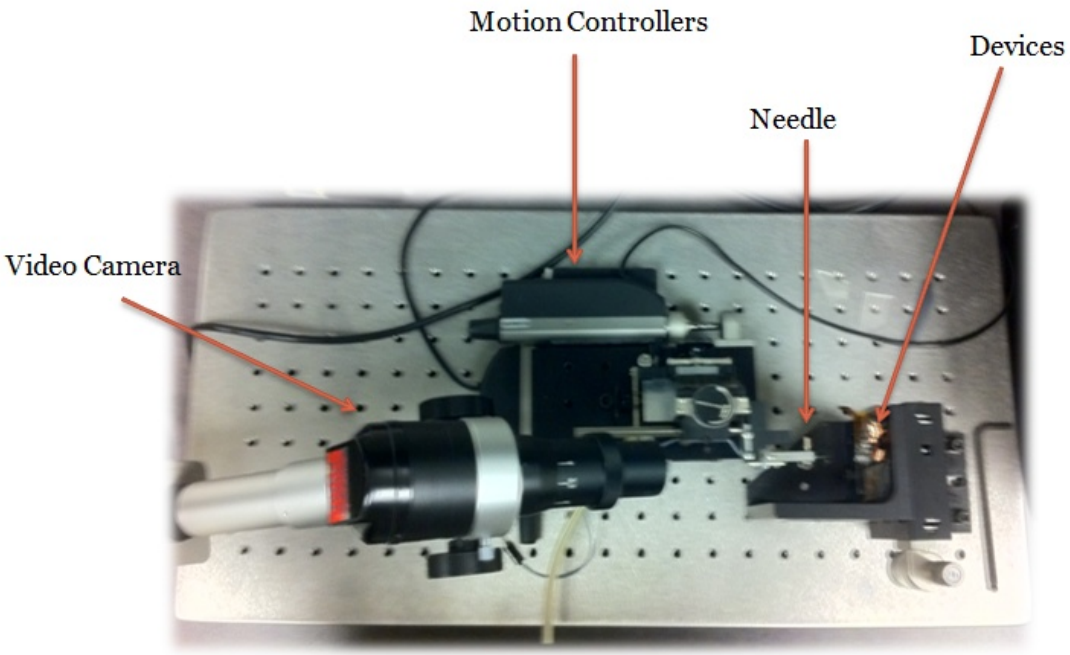

Figure 33 - Micro controlled motors test stand

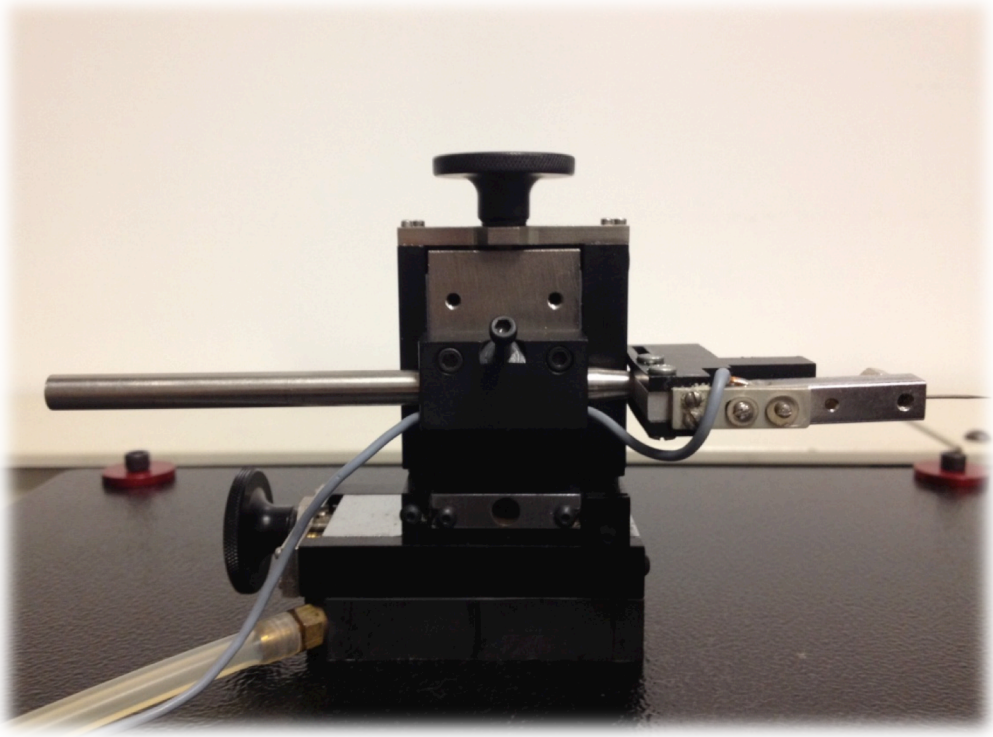

Figure 34 – Micromanipulator to hold the needle

4.2.3 Turntable Arm With Built In Micrometer

The next applied method involved the use of a Technics turntable arm for its pivot, which could be counter weighted in order to apply a specific force on the needle side (for music purposes this side plays the vinyl). The arm's counter weight couldn't be used because of the large change of weight per increment. Instead the back portion of the turntable arm was sawed off and a micrometer was fitted into the back end to provide smaller increments of weight to choose from. Micrometers are naturally used for measuring the inside or outside diameters of small parts. They are accurate measuring devices with precision commonly utilized to measure to the nearest one thousandth of an inch. Micrometers are made up of several different parts, including the spindle, spindle face, sleeve, and thimble.

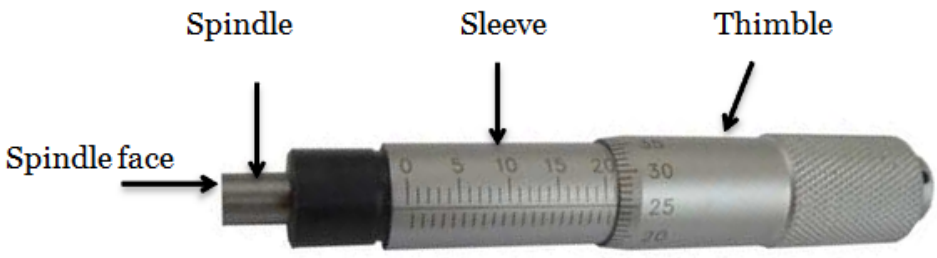

Figure 35 - Micrometer for counterweight

The micrometer naturally weighed more than the original counter weight, thus I needed to find something that could counter the weight of the micrometer and be able to hold a stylus needle. This would eventually apply the force on the micro-hinge. A pipe coupling lock nut seemed to fit perfectly where the cartridge head for the turntable arm was affixed, and with minimal assistance from the Industrial Manufacturing Engineering (IME) department we drilled a small enough hole in the stainless steel piece to hold the

stylus needle. This process was very important to ensure the part that held the needle wasn't too heavy and also that the needle was directly perpendicular to the flat surface that the arm sat on. Also the hole needed to be slightly larger than the needle that sat in it, but not too large to where the needle would come loose after testing with it numerous times. The pivot that the arm would rotate on also needed to be adjusted so that there was little to no friction while testing. To overcome the friction issue, graphite was applied inside the pivot which eliminated the friction.

Figure 36 - Turntable arm with built in micrometer

A small mirror was then attached to the top part of the stainless steel piece of the arm so a HeNe laser could be focused on it. During testing the laser could reflect off the mirror into a PSD to read the amount of rotation that the micro-hinge endured. The rest of the test stand was created using ThorLabs equipment including Newport 443 stage, 423 stage, and M360-90°mount. In order to position the devices directly below the needle, two stages were operated with Newport Universal Motion Controller which controlled the X and Y direction. A third motion controller was used to control the turntable arm by pushing down on the micrometer end to raise or lower the needle, which allowed the needle to be gently placed on the edge of the devices being tested. It was important to use this controller because attempting to set the needle on the device by hand would

cause damage to the devices, and it worked as a good damping mechanism. The crucial element to the motion controllers was the capability to move only 0.00004mm per click which made the positioning and damping very precise. The PSD needed to be positioned and angled directly in line with the HeNe laser that was reflected off the mirror which was attached to the turntable arm. The PSD was attached to a M360-90° angle mount which was then titled forward onto the two columns that held it in position, with an additional support mount to hold the back part of the M360-90° angle mount. The laser beam needed to be directly in line with the PSD because the face of the detector has a potential applied in both the vertical and horizontal directions. This allowed the PSD to detect movement in both the X and Y directions, up to 30mm in either direction. Once the laser strikes the PSD face, electron-hole pairs are created which are swept away by an applied potential bias. The separation of electron and hole creates a potential which can then be measured. The locations of the detected electron-hole pairs from the laser spot are averaged and outputted as a voltage. If the laser spot moves in a vertical direction, the potential will change. This voltage ranges from -10V to 10V and changes linearly with movement in the vertical direction.

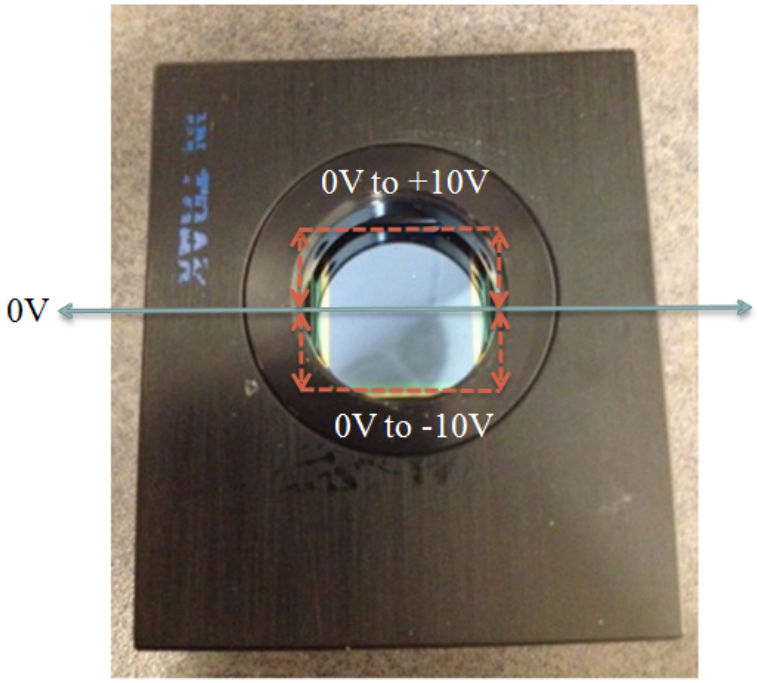

Figure 37 - PSD with top half ranging (0V to +10V) and bottom half ranging (0V to -10V)

As the laser travels from the center blue line upward in (shown in Figure 37), the voltage will increase to a maximum of ten volts and if it were to travel below the blue line it would decrease to a maximum of negative ten volts. The data that is collected from the PSD is sent through a signal amplifier called OT-301 Precision Position sensing amplifier that has six gain features, which can accommodate input current ranges from 0.1μA to 1.5Ma with a frequency response to 15 kHz. The output signal was connected to an Agilent 34405A Digital Multimeter which displayed a DC voltage output. The sensing amplifier was also connected to an Agilent 54622A Ocilloscope to determine the amount of noise that was in the output signal by observing a DC voltage waveform.

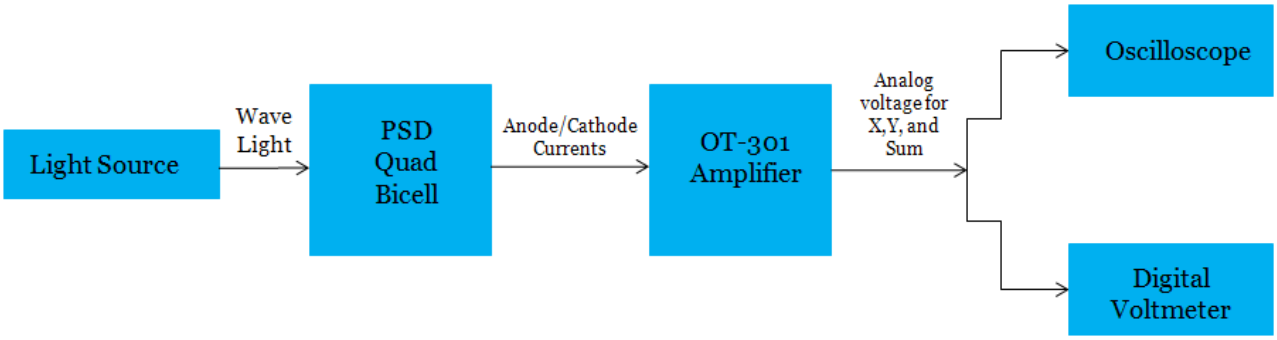

Figure 38 – Output capability diagram

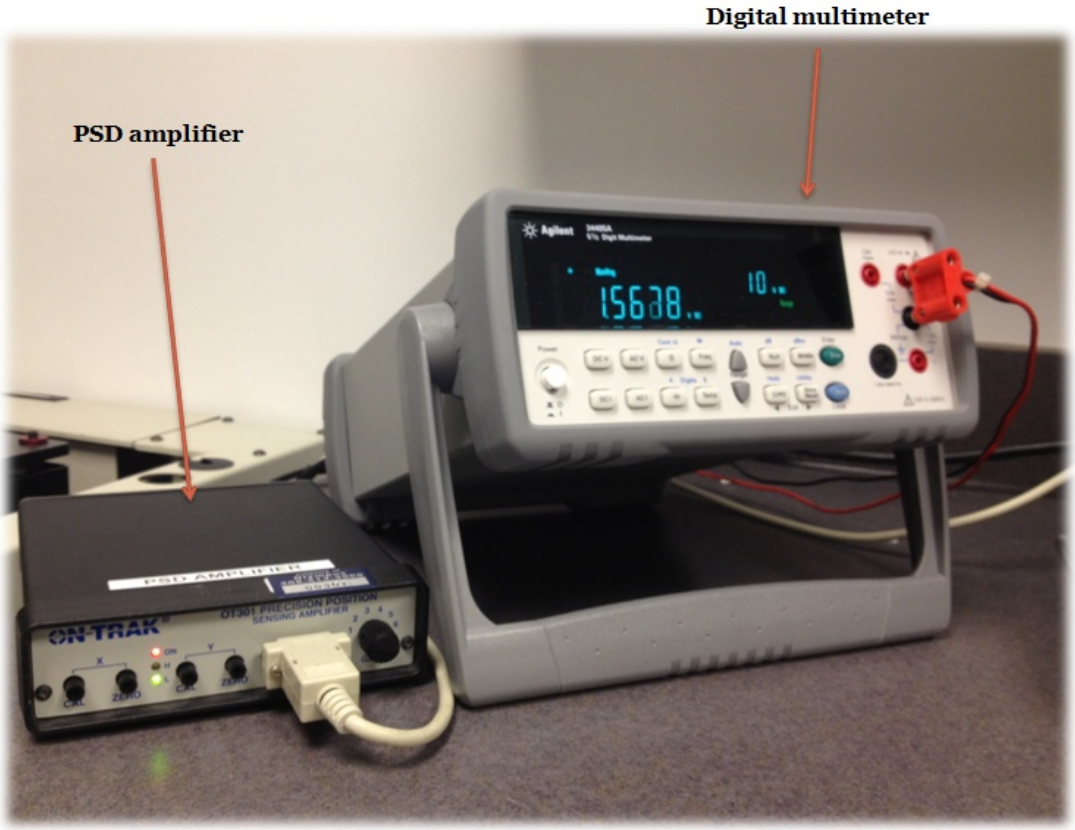

Figure 39 - PSD amplifier (left) and digital multimeter (right)

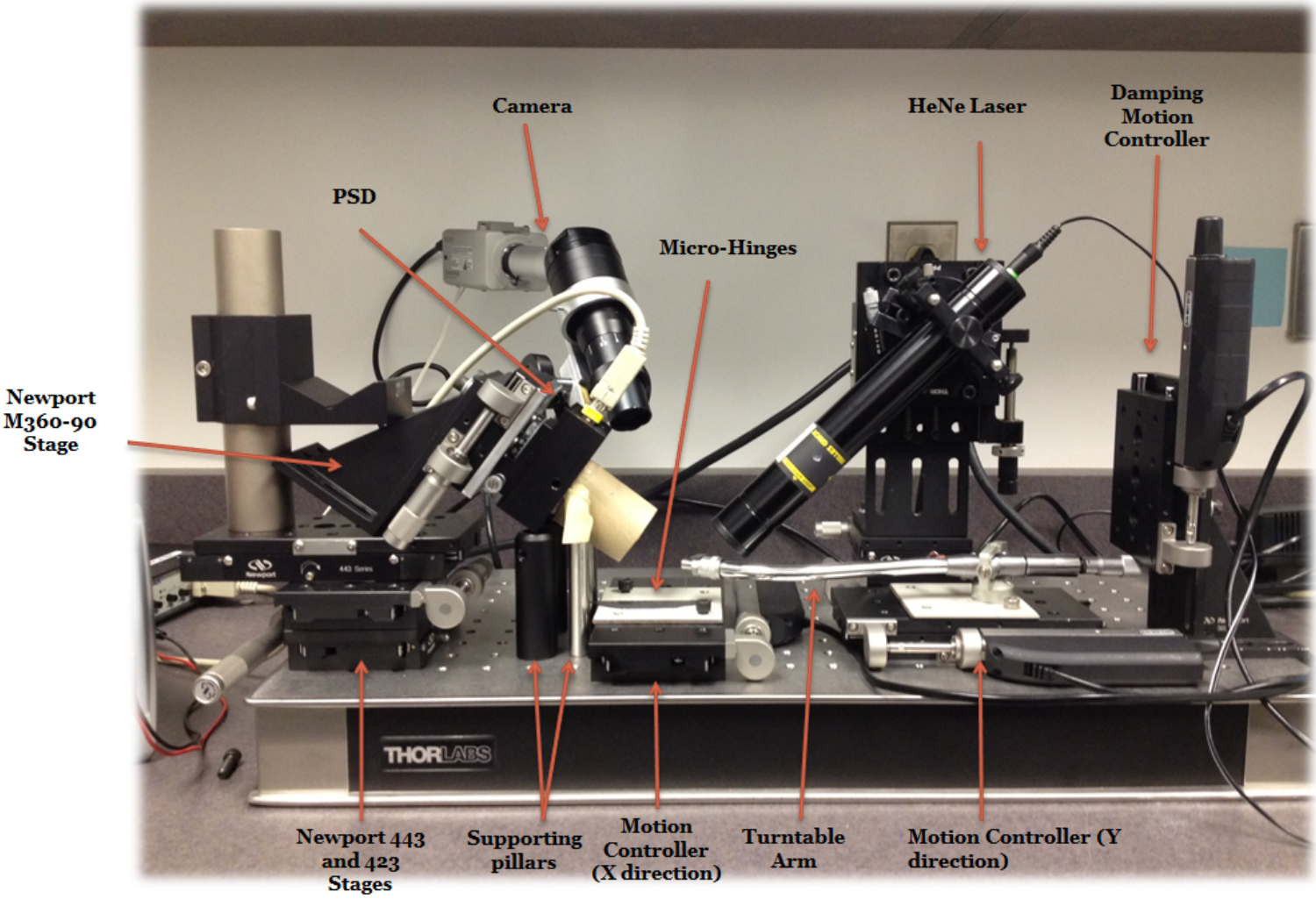

Figure 40 – Turntable arm with built in micrometer test stand

The turntable arm was characterized using Mettler AE 160 scale by rotating the micrometer in increments of thousandths of an inch and recording the amount of weight displayed. This method was checked numerous times to ensure the repeatability of the arm and to check for any variations that might be a factor while testing the devices.

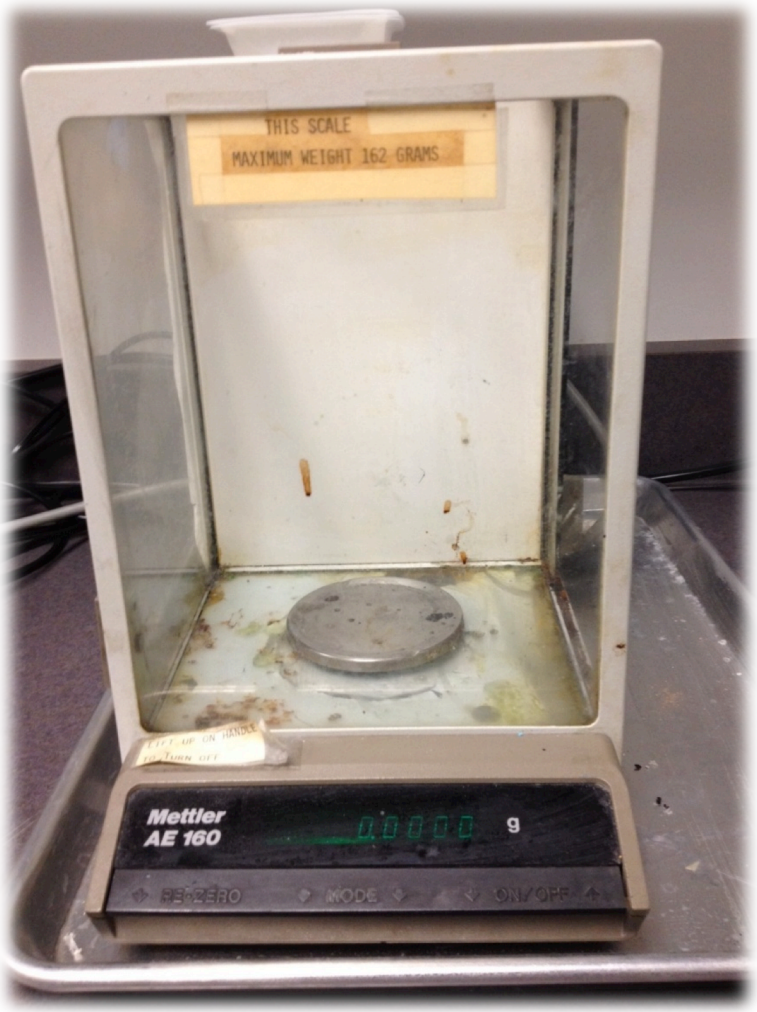

Figure 41 - Mettler AE 160 micro scale to calibrate turntable arm

Table V - Calibration of turntable arm using microgram scale part 1

Micrometer Increments	4.00 mm	3.99 mm	3.98 mm	3.97 mm	3.96 mm	3.95 mm
1)	0.000152003 g	0.000172 g	0.000141 g	0.000193 g	0.000205 g	0.000264 g
2)	8.62985E-05 g	0.00015 g	0.00019 g	0.000237 g	0.000286 g	0.00022 g
3)	1.7652E-05 g	6.47E-05 g	0.00011 g	0.000144 g	0.000199 g	0.000229 g
4)	3.72653E-05 g	7.55E-05 g	0.000125 g	0.000175 g	0.000197 g	0.000228 g
5)	3.72653E-05 g	7.65E-05 g	0.000121 g	0.00018 g	0.000222 g	0.000271 g
6)	6.47239E-05 g	0.000129 g	0.000121 g	0.000134 g	0.000227 g	0.000271 g
7)	4.21686E-05 g	5.59E-05 g	0.000122 g	0.000173 g	0.000216 g	0.000249 g
8)	5.78592E-05 g	8.43E-05 g	0.00014 g	0.000181 g	0.000196 g	0.000237 g
9)	3.04006E-05 g	8.14E-05 g	0.000121 g	0.000164 g	0.000203 g	0.000228 g
10)	2.942E-05 g	7.45E-05 g	0.000112 g	0.000154 g	0.000179 g	0.000214 g
Average	5.55056E-05 g	9.63994E-05 g	0.00013 g	0.000174 g	0.000213 g	0.000241 g

Table VI - Calibration of turntable arm using microgram scale part 2

Micrometer Increments	3.94 mm	3.93 mm	3.92 mm	3.91 mm	3.90 mm	3.89 mm
1)	0.000329 g	0.000276548 g	0.00032 g	0.000334 g	0.000357 g	0.000394 g
2)	0.000243 g	0.000268702 g	0.000301 g	0.000321 g	0.000346 g	0.000383 g
3)	0.000263 g	0.000270664 g	0.000307 g	0.000331 g	0.000353 g	0.000381 g
4)	0.000258 g	0.000288316 g	0.000319 g	0.000328 g	0.000358 g	0.000387 g
5)	0.000289 g	0.000286354 g	0.0003 g	0.000342 g	0.00037 g	0.000398 g
6)	0.000316 g	0.000288316 g	0.000315 g	0.000332 g	0.00037 g	0.000392 g
7)	0.00028 g	0.000282432 g	0.000309 g	0.000334 g	0.000373 g	0.000392 g
8)	0.000277 g	0.000297141 g	0.000328 g	0.000333 g	0.000367 g	0.000388 g
9)	0.000265 g	0.000269683 g	0.000311 g	0.000341 g	0.000371 g	0.000395 g
10)	0.000243 g	0.000283412 g	0.000323 g	0.000323 g	0.000341 g	0.000391 g
Average	0.000276 g	0.000281157 g	0.000313126 g	0.000332 g	0.00036 g	0.00039 g

Table VII - Calibration of turntable arm using microgram scale part 3

Micrometer Increments	3.88 mm	3.87 mm	3.86 mm	3.85 mm	3.84 mm	3.83 mm
1)	0.000413 g	0.000433 g	0.000451 g	0.000483 g	0.000513868 g	0.000540346 g
2)	0.000402 g	0.000435 g	0.000433 g	0.000478 g	0.000511907 g	0.000541327 g
3)	0.000398 g	0.000431 g	0.000446 g	0.000482 g	0.000512888 g	0.000533482 g
4)	0.000393 g	0.000431 g	0.000448 g	0.000482 g	0.000518772 g	0.000551134 g
5)	0.000401 g	0.00043 g	0.000467 g	0.000489 g	0.000522694 g	0.000548192 g
6)	0.000409 g	0.000438 g	0.000451 g	0.000477 g	0.000508965 g	0.000543288 g
7)	0.000413 g	0.000445 g	0.00047 g	0.000479 g	0.000509946 g	0.000537404 g
8)	0.000409 g	0.00043 g	0.000449 g	0.000477 g	0.000509946 g	0.000538385 g
9)	0.000415 g	0.00045 g	0.000469 g	0.000482 g	0.000513868 g	0.000544269 g
10)	0.000415 g	0.000425 g	0.000464 g	0.000482 g	0.000512888 g	0.00054525 g
Average	0.000407 g	0.000435 g	0.000455 g	0.000481 g	0.000513574 g	0.000542308 g

Table VIII - Calibration of turntable arm using microgram scale part 4

Micrometer Increments	3.82 mm	3.81 mm	3.80 mm	3.79 mm	3.78 mm	3.77 mm
1)	0.000557 g	0.000564 g	0.000580554 g	0.000599186 g	0.00062 g	0.00064822 g
2)	0.000555 g	0.000566 g	0.000579573 g	0.000598206 g	0.000619 g	0.000596244 g
3)	0.000558 g	0.000567 g	0.000587418 g	0.000601148 g	0.000621 g	0.00058938 g
4)	0.000559 g	0.000567 g	0.000588399 g	0.000599186 g	0.000623 g	0.000639394 g
5)	0.000562 g	0.000562 g	0.000581534 g	0.000606051 g	0.000618 g	0.000621742 g
6)	0.000557 g	0.000568 g	0.000579573 g	0.00060409 g	0.00062 g	0.000599186 g
7)	0.000555 g	0.000559 g	0.000579573 g	0.000597225 g	0.000616 g	0.000602128 g
8)	0.00056 g	0.000562 g	0.000580554 g	0.000591341 g	0.000623 g	0.000599186 g
9)	0.000561 g	0.000564 g	0.000585457 g	0.000599186 g	0.000615 g	0.00058938 g
10)	0.000561 g	0.000566 g	0.000578592 g	0.000600167 g	0.000623 g	0.000595264 g
Average	0.000558 g	0.000564 g	0.000582123 g	0.000599579 g	0.00062 g	0.000608012 g

Table IX - Calibration of turntable arm using microgram scale part 5

Micrometer Increments	3.76 mm	3.75 mm	3.74 mm	3.73 mm	3.72 mm	3.71 mm
1)	0.000664 g	0.000702 g	0.000718 g	0.000998 g	0.001285 g	0.001615 g
2)	0.000634 g	0.000659 g	0.000693 g	0.001028 g	0.001222 g	0.001565 g
3)	0.000653 g	0.000704 g	0.000738 g	0.001001 g	0.001302 g	0.001575 g
4)	0.000665 g	0.000674 g	0.000742 g	0.000996 g	0.001279 g	0.001554 g
5)	0.000668 g	0.000688 g	0.000703 g	0.000999 g	0.001286 g	0.001601 g
6)	0.000606 g	0.000668 g	0.000722 g	0.000998 g	0.001285 g	0.001582 g
7)	0.000656 g	0.000678 g	0.000735 g	0.001099 g	0.001310 g	0.001579 g
8)	0.00064 g	0.000663 g	0.000694 g	0.001011 g	0.001299 g	0.001566 g
9)	0.000646 g	0.000679 g	0.000708 g	0.000997 g	0.001300 g	0.001598 g
10)	0.000632 g	0.00068 g	0.000704 g	0.000995 g	0.001293 g	0.001587 g
Average	0.000646356 g	0.000679 g	0.000716 g	0.0010122 g	0.001286 g	0.0015822 g

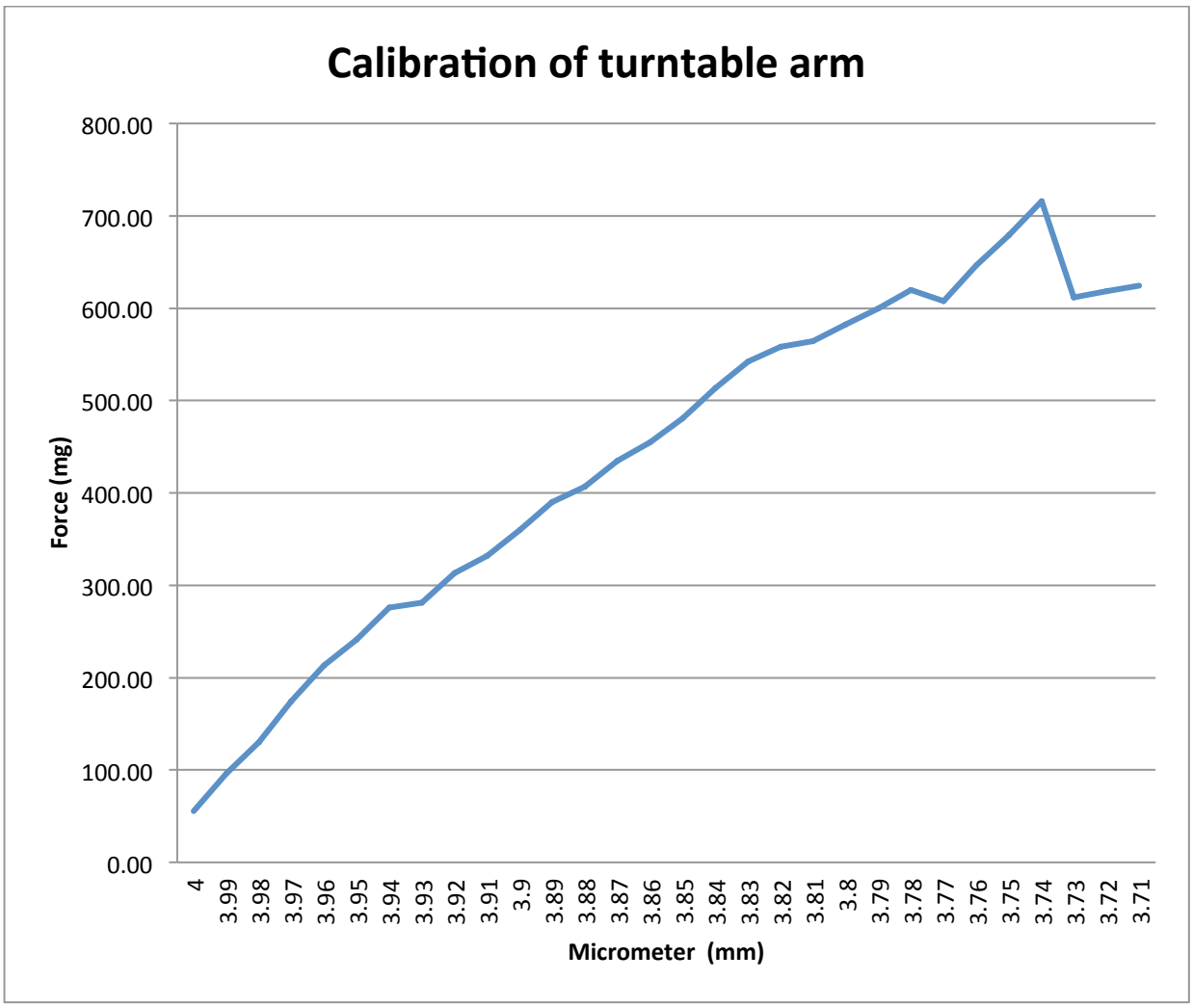

Figure 42 - Calibration of turntable arm

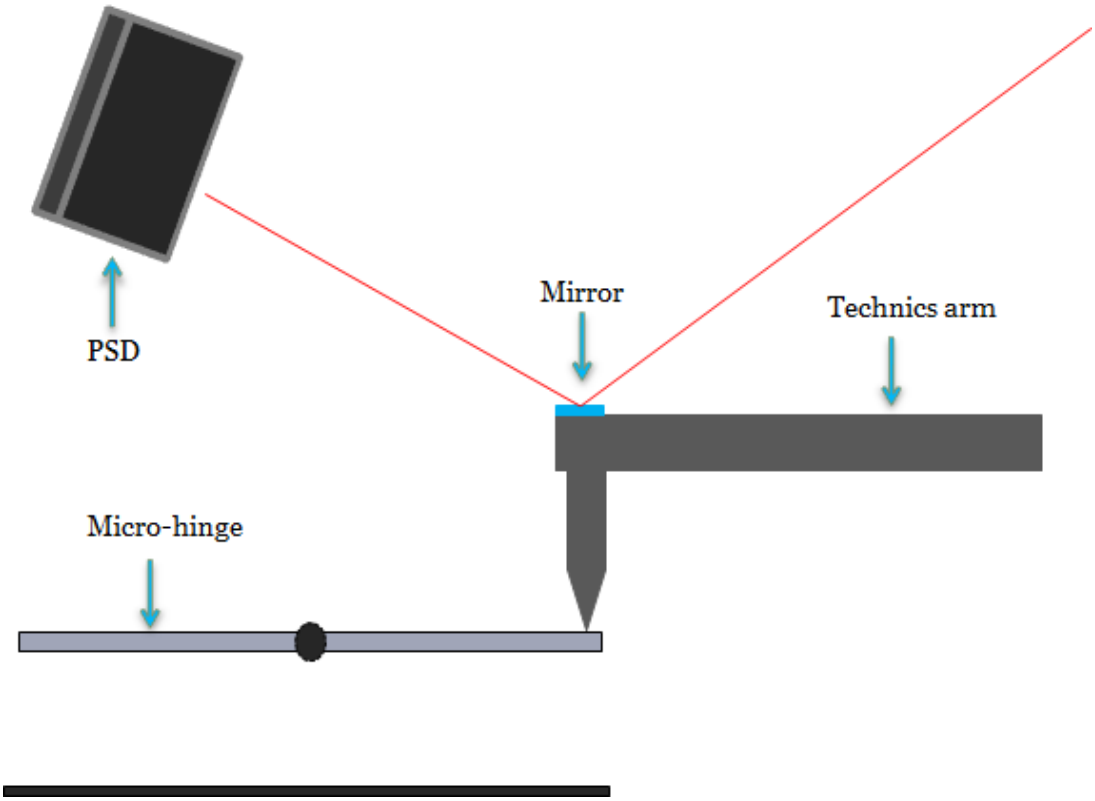

Figure 43 - Test stand with no force applied

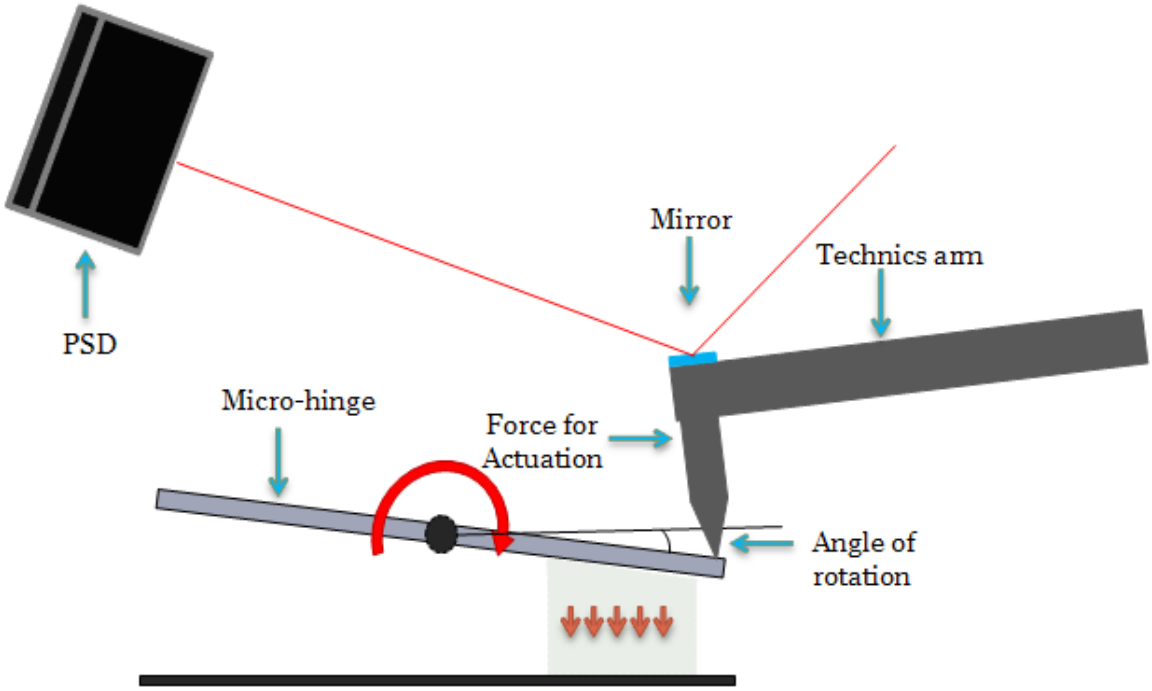

Figure 44 - Test stand with applied force

This technique gave me a rotational angle, but it seemed to measure more of the displacement of the Technics arm than the rotation of the micro-hinge. It was determined that the mirror should be positioned not on the end of the arm but at the pivot of the arm. This approach utilized the same test stand as before but required the PSD to be raised much higher in order to be in line with the incoming HeNe laser which was reflected off the mirror positioned at the pivot. Several supporting pillars were screwed together to raise the PSD to the required height. While testing, scattering light seemed to be an issue and caused the digital multimeter to vary ±.5v per test. The first approach to alleviate this problem was to mask off the windows to the AFM lab with black garbage bags and turn off all the lights while testing. This proved to help with some of the varying voltages but the output signal never seemed to stabilize. After talking to Dr. Sharpe in the Physics department he suggested using a HeNe band past filter to allow only the HeNe laser to hit the PSD and filter out all other wavelengths in the room. This allowed for the output signal to stabilize and solved the problem of outside light disrupting the PSD while testing.

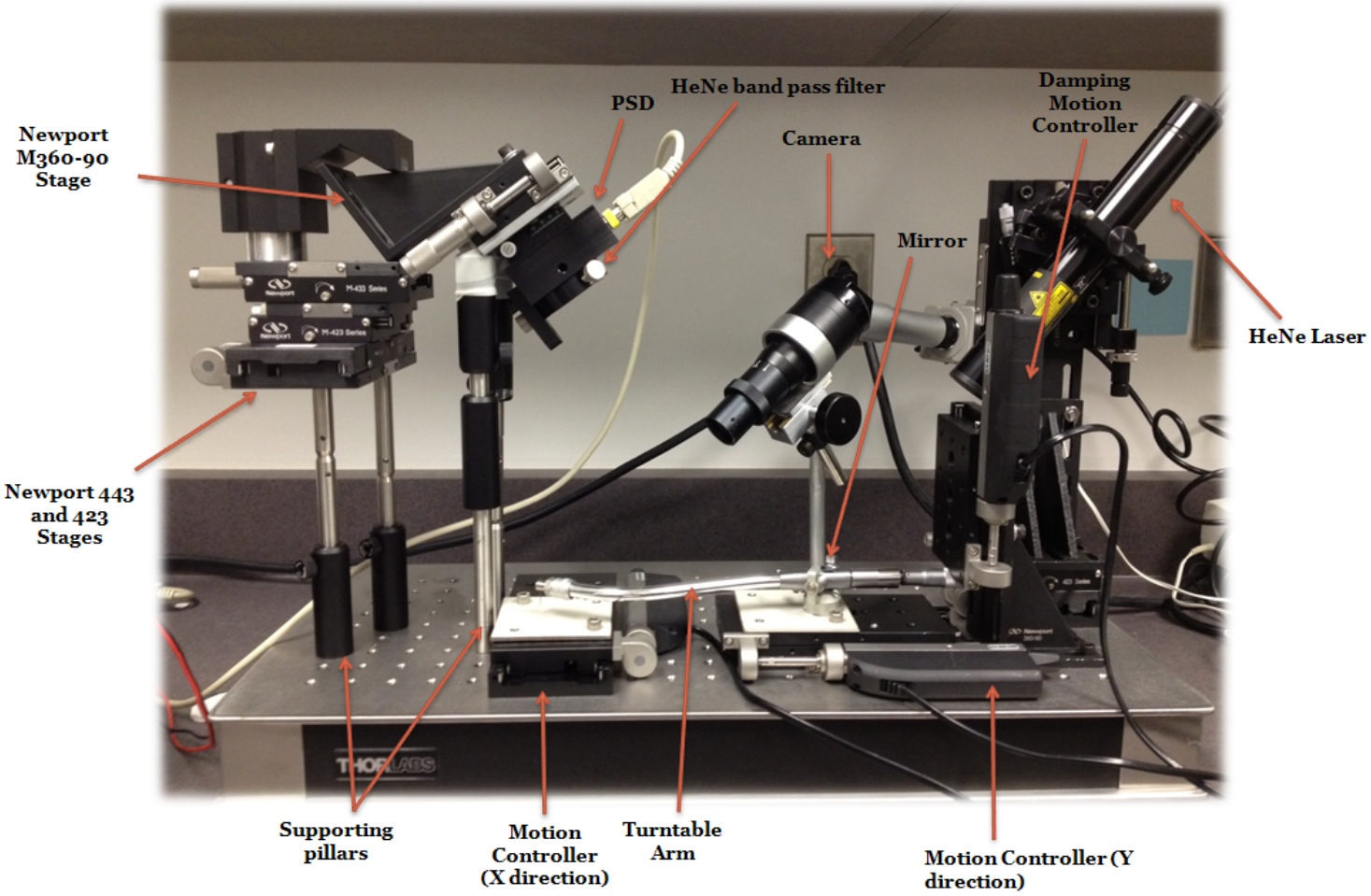

Figure 45 - Final test stand

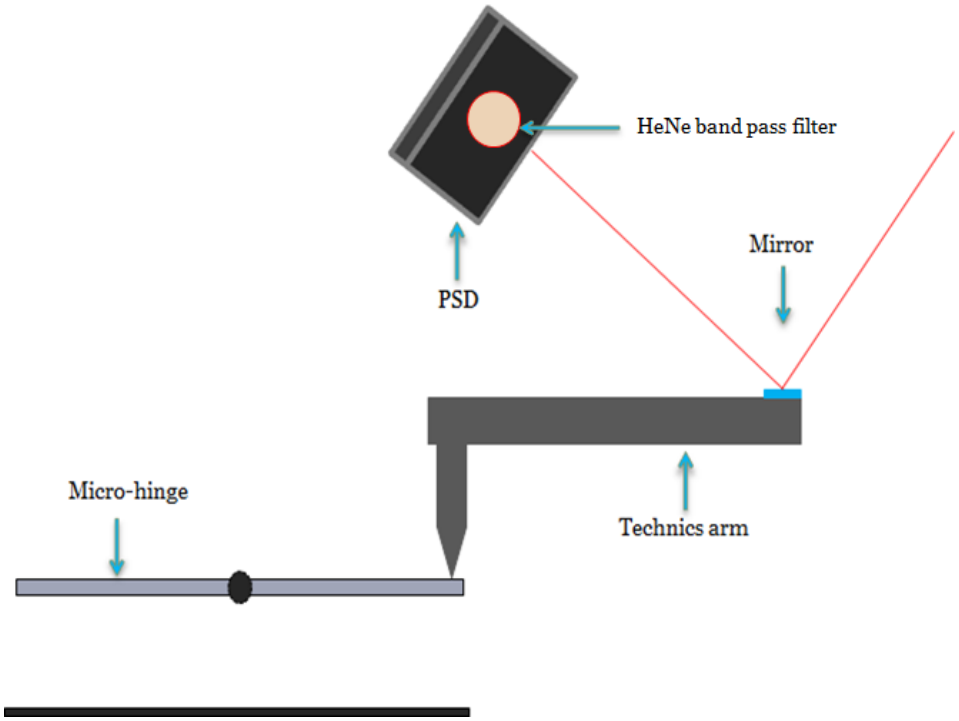

Figure 46 - Final test stand with no force applied

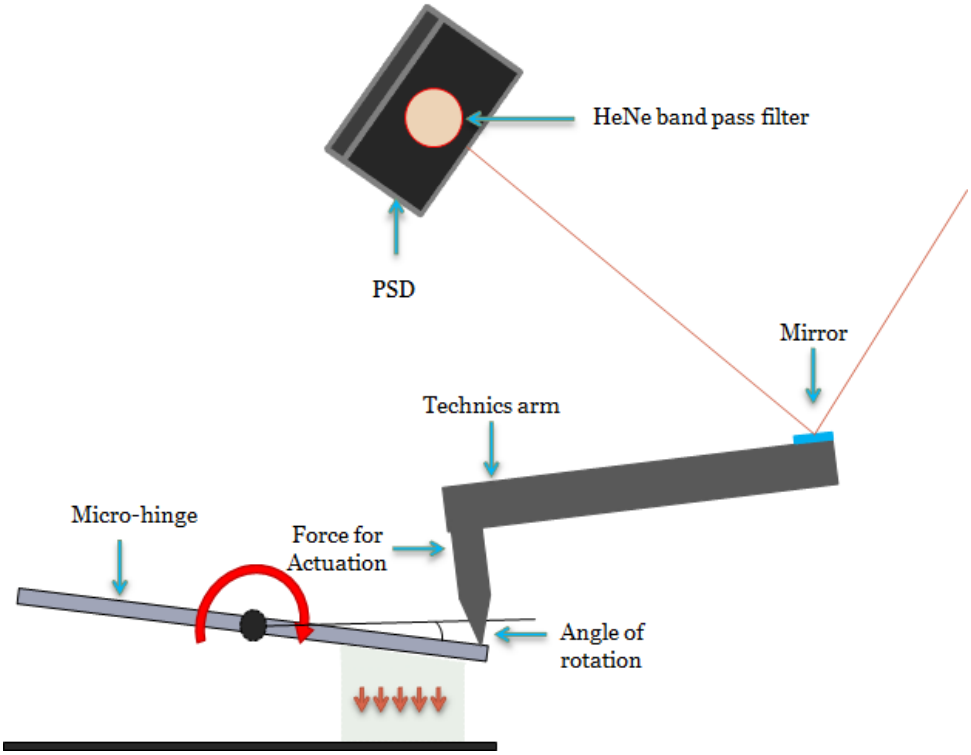

Figure 47 – Final test stand with applied force

The micro-hinges were successfully rotated and as the force increased the rotational angle also noticeably increased as well. Measurements were taken by positioning the needle 0.5mm above the micro-hinge being tested and recording the voltage displayed by the digital multimeter (this was considered position zero). To insure position zero was always 0.5mm above the micro-hinge, the motion controller was programmed to home the needle at 0.5mm which allowed positioning to be exact every time. The force was then applied to the micro-hinge and the voltage difference between position zero and applied force position provided the voltage difference. This voltage difference was the amount of movement that the laser shifted on the PSD face. Also the amounts that the micrometer changed were so small that there wasn't much change in output voltage. Thus opposed to changing the micrometer by 0.01mm which is 0.000041g per test, it was changed 0.03mm which is 0.00075g per measurement. Each wafer had a total of 153 devices, and a total of 252 devices (equivalent to one and a half wafers) were measured with ten different amounts of force.

Table X - Average output voltage from digital multimeter

	Force Applied (µN)	**Position Zero (V)**	**Applied Force (V)**	**Difference (V)**	**Displacement (µm)**	**Angle of rotation (degrees)**
1	0.544	1.08	1.09	0.01	2.49	0.79
2	1.70	1.09	1.11	0.02	4.50	1.43
3	2.70	1.08	1.13	0.05	8.26	2.63
4	3.25	1.08	1.17	0.09	15.90	5.06
5	3.99	1.09	1.20	0.11	28.70	9.13
6	4.71	1.09	1.23	0.14	35.79	11.39
7	5.47	1.09	1.28	0.19	43.72	13.91
8	5.87	1.09	1.30	0.21	50.67	16.12
9	6.33	1.08	1.32	0.24	60.26	19.18
10	9.04	1.09	1.35	0.26	71.79	22.85

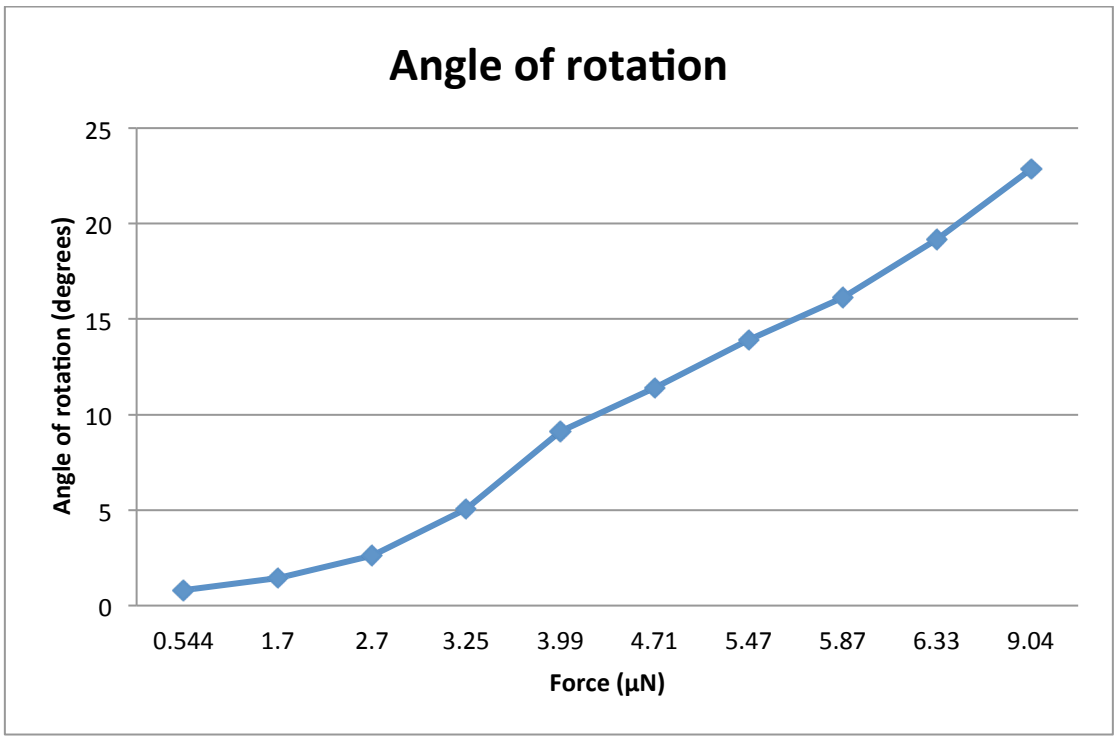

Figure 48 - Average angle of rotation on micro-hinges

Forces beyond 9.04µN the hinges started to exhibit deformation and caused some micro-hinges to snap. Some of the micro-hinges could handle slightly more force than others and this could have been due to the hinge thickness which varied cause of the fluctuating silicon etch rates.

4.2.4 Calibration of PSD and Determining an Angle of Rotation

It was necessary to calibrate the PSD in order to determine a rotational angle from the data that was being sent through the PSD and outputted to the digital mulitmeter which was in volts. Since I had a voltage difference between position zero and applied force, the distance that the laser traveled on the PSD could be determined using a motion controlled stage and HeNe laser in line with the PSD. The voltage will only change on the PSD if the laser travels up or down in the Y-direction and the change in voltage will correspond to the distance the laser traveled while applying a force. The laser was

positioned directly in line with the PSD which was mounted to a motion controlled stage. The motion controller was then moved in the Y-direction until the change of voltage matched the voltage difference that was witnessed during testing. This distance would allow me to determine an angle of rotation using trigonometry and small angle approximations.

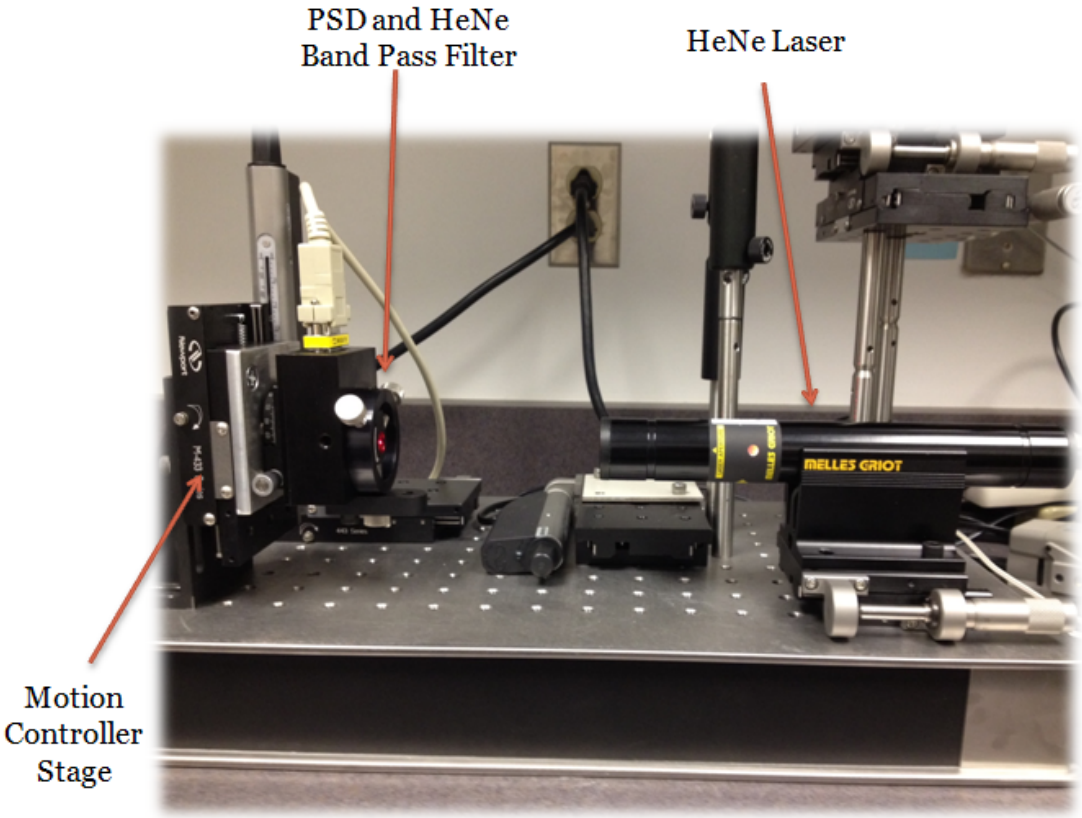

Figure 49 - Calibration of PSD

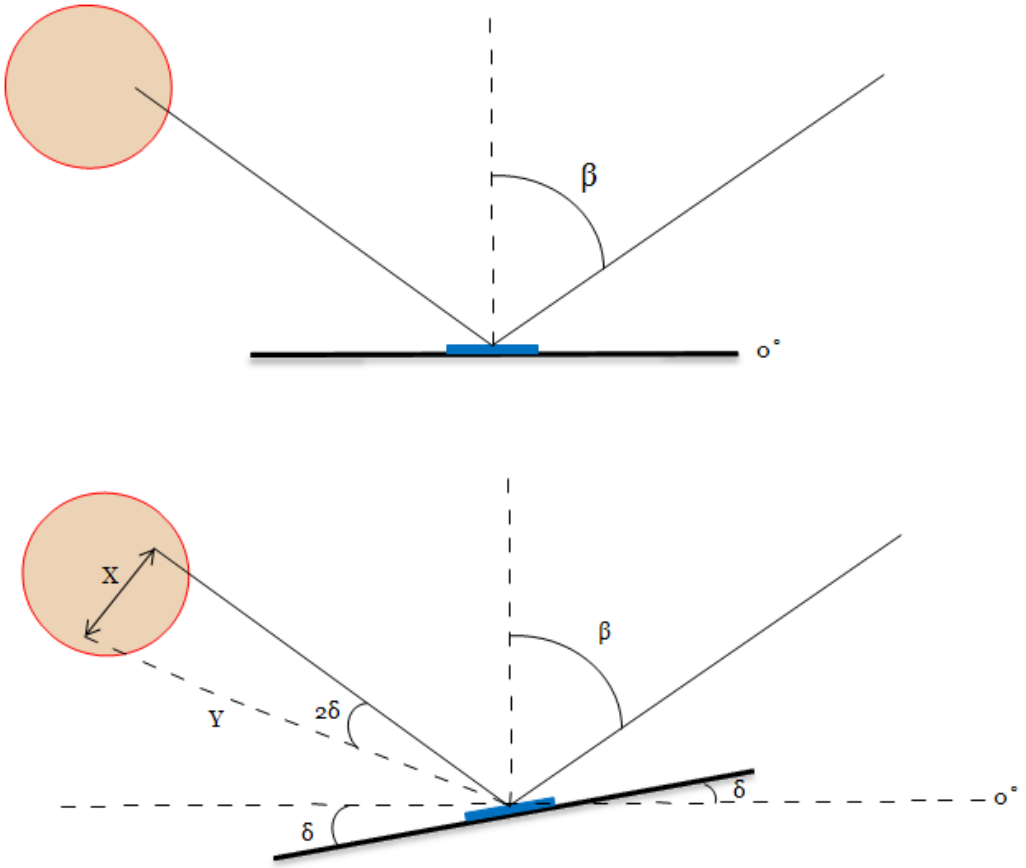

Figure 50 - Change in distance from position zero to applied force position on PSD

In the figure above X was the distance the laser travels during testing, β was the angle of incidence (AOI), δ is the angle of rotation that the turntable arm feels, and Y is the distance from the mirror mounted on the turntable arm to the PSD. Through small angle approximations the distance that the laser moves during testing could be determined which is X in Figure 48.

$$X = Y(2\delta) \tag{5}$$

Equation 4 was then related to the amount of distance the turntable arm traveled downward in the Y-direction.

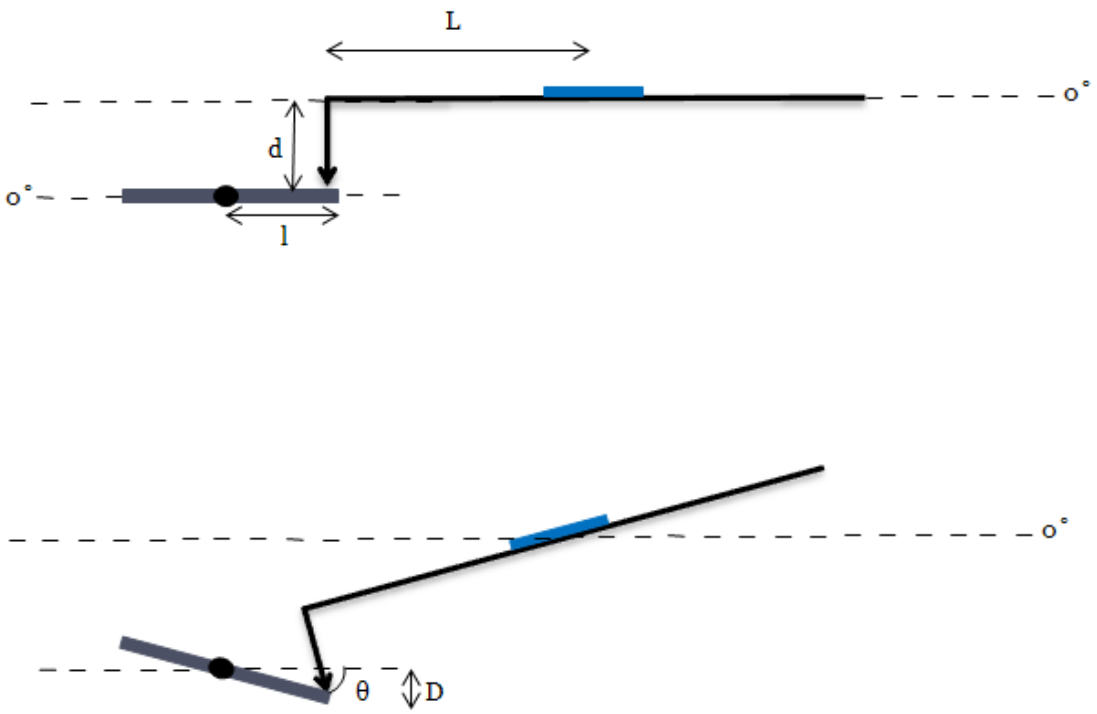

Figure 51 - Determining angle of rotation through the displacement of micro-hinge

$$D = L\delta \tag{6}$$

In Figure 49, L was the length of the turntable arm from the mirror to the needle, d is the length of the needle at position zero, l is the length of the micro-hinge from the hinges to the end, and θ is the angle of rotation that the micro-hinge endures. By combining Equation 5 and Equation 6 the distance traveled from position zero to the applied force in the Y-direction could be determined. This can be seen in Equation 7 below.

$$D = \frac{LX}{2Y} \tag{7}$$

With this displacement D, an angle of rotation θ could be determined by using a small angle approximation.

$$\theta = \left(\frac{D}{Y}\right)\left(\frac{180°}{\pi}\right) \tag{8}$$

The angle of rotation seemed to increase as more force was being applied which was expected. The reason that Equation 7 needed to be multiplied by 180° divided by π was to convert from radians to degrees.

SECTION 5: REPEATABILITY OF THE MICRO-HINGE

Since the hinges need to be repeatable the importance of fully recoverable positioning after multiple uses was vital. Throughout numerous tests on multiple devices, each micro-hinge proved to be very repeatable with various forces applied. Most micro-hinges were able to actuate to a specific angle and return to their original state once the force was released. A few devices had some permanent deformation after applying a force, which could have been due to varying silicon hinge thickness. During the deep silicon etch in TMAH, some hinges etched further into the silicon which created a slightly thinner hinge structure varying between 10μm to 18μm. To avoid this problem in the future, Silicon on insulator (SOI) wafers are recommended to act as a silicon stop at a specific depth. When applying some of the smaller forces on the device, more repeatable angles were witnessed and the larger forces produced more fluctuating results. Although each test was conducted by applying the force in the same location, it was difficult to be certain of the exact location when using a camera as a reference. The positioning of the stylus over the hinge structure varied between 10μm to the left or right of the center part of the hinge. The varying placement of the stylus on the hinge could have added to the different results and introduced larger stresses on one side of the hinge than the other. The stresses on the hinge structure could be observed using Finite Element Analysis (FEA) techniques. The stresses prove to change largely if the force is applied more to the right or left of the hinge opposed to the center edge of the micro-hinge.

SECTION 6: FUTURE WORK

One recommendation would be to analyze how these micro-hinges act with different hinge designs, such as a serpentine hinge structure. This would involve performing a similar force versus displacement on a serpentine hinge structure, and determining how the stress is distributed across the device. Another idea would be to vary the thickness of these devices in a more controlled manner by using SOI wafers that have varying depths for the insulator. It has been proven that electrostatic actuations of these devices are difficult to design. One could actuate these devices using similar techniques by instead of only having one capacitive layer that pulls the wafer down, an additional capacitive layer could be created to push also from the opposite side. This could significantly increase the amount of rotation due to the push and pull effect that the hinge endures. The positioning of the capacitive layers can also be analyzed to prevent any leakage current while testing. Another idea for future work is to create alignment marks for the second mask, avoiding the need to punch out some of the membranes needed to align the mask with the wafer.

References

[1] Tai-Ran, Hsu. *MEMS and Microsystems: Design, Manufacture, and Nanoscale Engineering*. 2nd. Hoboken, New Jersey: John Wiley , 2008. 35-75. Print.

[2] Toshiyoshi, Hiroshi, and Hiroyuki Fujita. Electrostatic Micro Torsion Mirrors for an Optical Switch Matrix. *Journal of Microelectromechanical Systems*. 5.4 (1996): n. page. Print.

[3] Dobbelaere, Peter, Ken Falta, Li Fan, Steffen Gloeckner, and Susant Patra. Digital MEMS for Optical Switching. *IEEE Communications Magazine*. March 2002: 88-95. Print.

[4] Chen, Jinghong, Wendelin Weingartner, Alexi Azarov, and Randy Giles. Tilt-Angle Stabilization of Electrostatically Actuated Micromechanical Mirrors Beyond the Pull-In Point. *Journal of Microelectromechanical Systems*. 13.6 (2004): 988-996. Print.

[5] Bryzek, Peterson. Micromachines on the March. *IEEE Spectrum*. (1994): 20-31. Print.

[6] Maluf, Nadim, and Kurt Petersen. Bulk Micromachining of Silicon. *Proceedings of the IEEE*. 86.8 (1998): 1536-1551. Print.

[7] Varadan, VK. Microsensors, microelectromechanical systems (MEMS), and electronics for smart structures and systems. *Smart Materials and Structures*. 9.6 (2000): n. page. Print.

[8] Wood, D., J.S. Burdess, and A.J. Harris. Actuaters and their Mechanisms in Microengineering. *Proceedings of the IEEE Colloquium on Actuator Technology*. 110. (1998): 19-26. Print.

[9] Liu, Huiwen, and Bharat Bhushan. Bending and Fatigue study on a Nanoscale Hinge by an Atomic Force Microscope. *Institute of Physics Publishing*. 15. (2004): 1246-1250. Print.

[10] Butt, Hans-Jürgen, Brunero Cappella, and Michael Kappl. Force Measurements with the Atomic Force Microscope: Technique, Interperetation and Applications. *Surface Science Reports*. 59. (2005): 17-83. Print.

[11] Hopcroft, Matthew, William D. Nix, and Thomas W. Kenny. What is the Young's Modulus of Silicon?. *Journal of Microelectromechanical Systems*. 19.2 (2010): 229-236. Print.

[12] Senturia, Stephen D., Narayan Aluru, and Jacob White. Simulating the Behavior of MEMS Devices: Computational Methods and Needs. *IEE Computational Science & Engineering*. 4.1 (1997): 30-39. Print.

[13] Lin, L.Y., S.S. Lee, K.S.J. Pister, and M.C. Wu. Micro-machined three-dimensional micro-optics for integrated free-space optical system . *IEEE Photonics Technology Letters*. 6.12 (1994): 1445-1447. Print.

[14] Hao, Zhili. *MEMS/NEMS Handbook Techniques and Applications*. 1. Los Angeles: Springer Science, 2006. 329-386. Print.

[15] Kingon, Al, JP Maria, and SK Streiffer. Alternative Dielectrics to Silicon Dioxide for Memory and Logic Devices. *Nature*. 406. (2000): n. page. Print.

[16] Haque, M.A., and M.T.A. Saif. Microscale Materials Testing using MEMS Actuators. *Journal of Microelectromechanical Systems*. 10.1 (2001): 146-152. Print.

[17] Nielson, Gregory, and George Barbastathis. Dynamic pull-in of parallel-plate and torsional electrostatic MEMS Actuators. *Journal of Microelectromechanical Systems*. 15.4 (2006): 811-821. Print.

[18] Patton, S.T., and J.S. Zabinski. Failure mechanisms of a MEMSactuator in very high vacuum. *Tribology International*. 35.6 (2002): 373-379. Print.

[19] Gorthi, Subrahmanyam, Atanu Mohanty, and Anindya Chatterjee. Cantilever Beam Electrostatic MEMS Actuators Beyond Pull-in. *Journal of Micromechanics and Microengineering*. 16. (2006): n. page. Print.

[20] Senturia, Stephen D. CAD challenges for microsensors, microactuators, and microsystems . *Proceedings of the IEEE*. 86.8 (1998): 1611-1621. Print.

[21] Hirano, Toshiki, Tomotake Furuhata, Kaigham J. Gabriel, and Hiroyuki Fujita. Design, fabrication, and operation of submicron gap comb-drive microactuators . *Journal of Microelectromechanical Systems*. 1.1 (1992): 52-58. Print.

[22] Chesbro, Dylan. *Design, Fabrication, And Characterization of Electrostatically-Actuated Silicon Micro-Mirrors*. MS thesis. Materials Engineering-California Polytechnic State University, 2010. 2010. Print.

[23] Meredith, Steven. *Characterization of a Viscoelastic Response From This Metal Films Deposited on Silicon for Microsystem Applications*. MS thesis. Materials Engineering-California Polytechnic State University, 2009. 2009. Print.

Appendix A – Lithography Masks

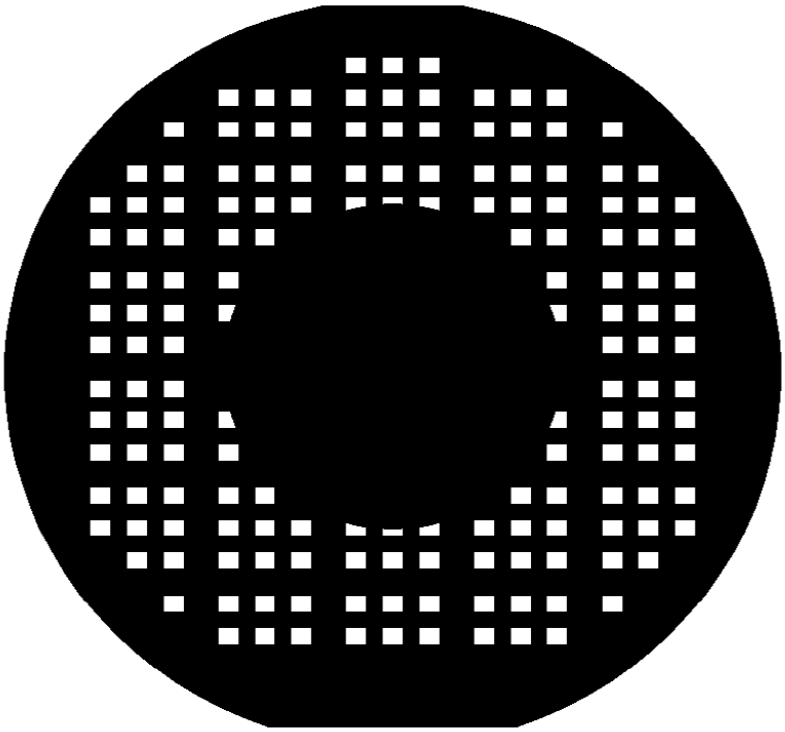

Figure 52 - Mask one to expose the wells

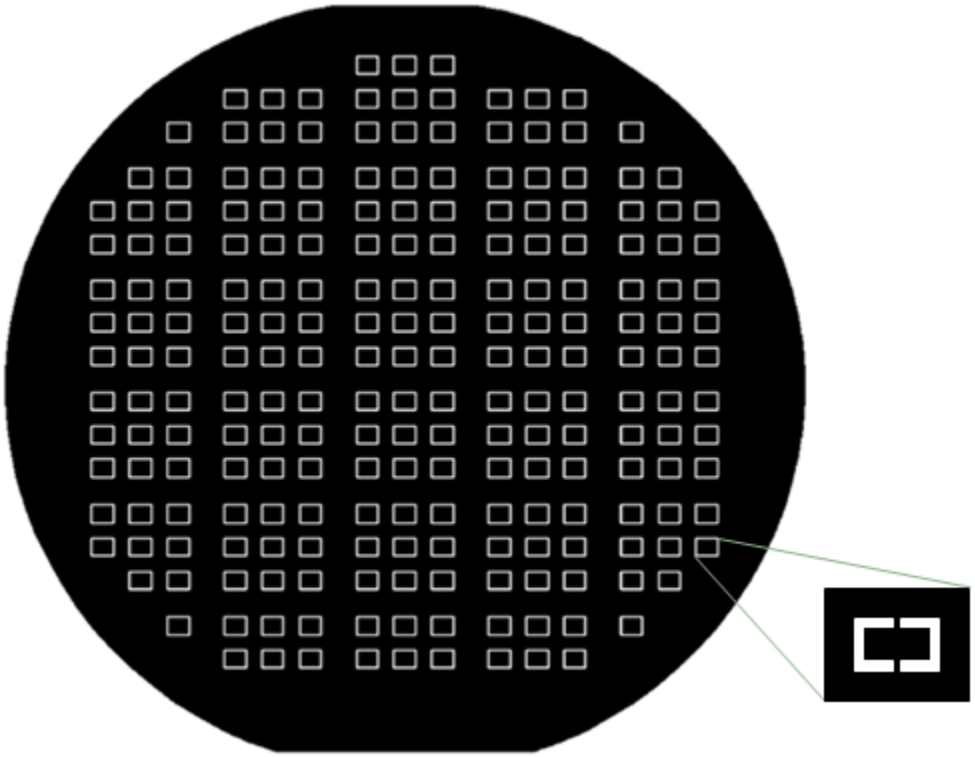

Figure 53 - Mask two to create the micro-hinges

Appendix B – Process Diagrams

Top View

Side View

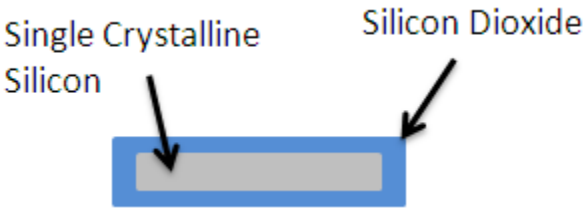

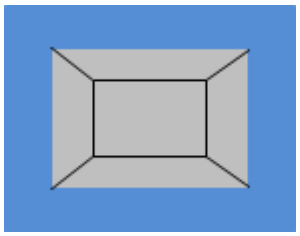

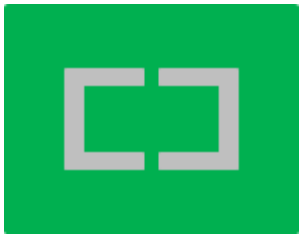

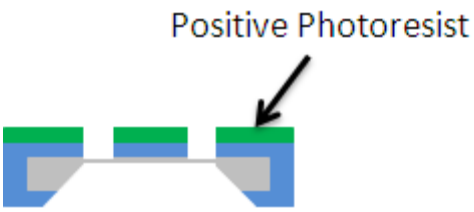
Positive Photoresist